THESIS

NEW INSIGHTS INTO FLOW OVER SHARP-CRESTED AND PIVOT WEIRS USING COMPUTATIONAL FLUID DYNAMICS

Submitted by

Joseph Sinclair

Department of Civil and Environmental Engineering

In partial fulfillment of the requirements

For the Degree of Master of Science

Colorado State University

Fort Collins, Colorado

Summer 2021

Master's Committee:

Advisor: Subhas Karan Venayagamoorthy
Co-Advisor: Timothy K. Gates

Xinfeng Gao

ABSTRACT

NEW INSIGHTS INTO FLOW OVER SHARP-CRESTED AND PIVOT WEIRS USING COMPUTATIONAL FLUID DYNAMICS

Irrigation for agriculture is the highest use of fresh water in the world. Efficient and equitable access and distribution of this water is vital to survival of the Earth's population. Open channels are the most common means of conveying water for agricultural irrigation and hydraulic structures are often used in these open channels to regulate and measure flow to achieve desired conditions. Sharp-crested weirs are one of the most popular of these structures and pivot weirs are quickly becoming a more widely used hydraulic structure. The purpose of this study was to reexamine both types of weirs to better understand how they operate for flow regulation and measurement and to provide insights into the flow structure around the weir. Computational fluid dynamics, or CFD, was the primary tool used, with a commercial code called FLOW-3D being the specific software selected.

Prior to investigating the weirs, preliminary studies were carried out to identify the best-practices in building an open-channel and hydraulic flow simulation in FLOW-3D. It was found that because FLOW-3D has no method of specifying developed flow prior to entering the model domain, additional care had to be taken to develop flow within the computational domain. The upstream length in the models was often extended to give the simulated flow more time and distance to develop. Additionally, the first-cell height had to be within a certain dimension to produce accurate velocity profiles due to the use of the logarithmic law of the wall boundary condition to solve for velocity in the first cell. Finally, a study analyzing the effects of the

simulated downstream distance after a free-flowing sharp-crested weir revealed that the downstream distance has no effect on upstream flow.

The sharp-crested weir parametric study analyzed velocity and pressure profiles over the crest, several calculated discharge coefficients, and turbulence flow structures upstream of the weir using high-resolution two-dimensional simulations. Three distinct operating regimes were identified based on the profiles over the crest as well as plots of the discharge coefficient against h/P where h is the upstream potentiometric head above the weir crest and P is the height of the crest above the channel bed. The first regime, the high-acceleration regime, occurs when $h/P < 0.6$. Flow accelerates greatly near the weir crest which results in negative pressure. The discharge coefficient has a negative linear trend with h/P in this regime. The next region occurs where $0.6 < h/P < 2.0$ and is called the ideal-operating regime. In this regime, flow is not experiencing acceleration or inundation and better maintains the assumptions used in deriving the classical rating equation. The discharge coefficient is relatively constant in this case and a single value can be used with minimal error for all flow rates within this range. The final regime, the weir-inundated regime, is where $h/P > 2.0$. The weir is often submerged here and the effect of the weir on the flow is diminished due to the high depth of flow. Turbulence patterns upstream of the weir appear to have a relationship to the Reynolds number, *Re*, of the flow with eddies reaching a minimum size at a $Re = 70{,}000$. The region of smallest eddy size correlated to the ideal-operating regime, again lending to the hypothesis that flow is more efficiently controlled within this regime.

Six flow rates at five different gate angles (27°, 47°, 57°, 72°, and 90°) were tested for the pivot weir study. After analysis of the h/P values and discharge coefficients, it was found that the flow rates bounding the ideal-operating regime shift lower in magnitude as the gate angle decreases.

Each angle also has an associated relatively constant discharge coefficient in its ideal-operating regime, meaning a single coefficient value may be used with minimal error. Comparison of the average discharge coefficient for each angle revealed a minimum value at 72° and a maximum value at 27°. The fraction of the total upstream mechanical energy head comprised of the velocity head was found to increase as gate angle decreased. Visual contours of velocity and pressure depicted how the flow changes as it approaches weirs of varying angles, with the recirculation zone moving from upstream of the weir to solely downstream of the weir for angles below 47°. Plots of the non-dimensional pressure and velocity profiles over the weir crest revealed that velocity over the crest increases as the inclination angle decreases. At the 47° weir, the flow acceleration created a region of negative relative pressure close to the weir.

These results highlight how flow over both the sharp-crested weir and pivot weir varies considerably. Thus, caution must be exercised in using empirical discharge coefficients for a broad range of *h/P* value.

ACKNOWLEDGMENTS

First, I would sincerely like to thank my advisor Dr. Karan Venayagamoorthy for allowing me to study under him and providing me with incredible guidance. His support as both an educator and mentor have made me a better student, engineer, and person and I will cherish the time I had in this program.

I would also like to acknowledge Dr. Timothy Gates, my co-advisor, for his continued support on this project. Working as a graduate student under a professor I had as an undergrad was a special experience and his knowledge will stay with me throughout my career.

I wish to show my appreciation for Dr. Xinfeng Gao for agreeing to be my committee member and review my work. I am grateful for the helpful comments, mentorship, and advice provided.

This work was supported by the Colorado Agricultural Experiment Station under grant no. COL00788.

To the graduate students of the Environmental Fluid Mechanics Laboratory, I want to extend my gratitude for welcoming me into the lab and for the wonderful friendships that were made during this time.

Finally, I want to thank all my family and my friends for their continued support and love through this journey. In particular, I would like to especially thank my parents for their unwavering support and care throughout my life that has help me become the man I am today.

TABLE OF CONTENTS

LIST OF TABLES

LIST OF FIGURES

CHAPTER 1 – INTRODUCTION

1.1 - Overview

In a world where water is becoming a scarce and valuable resource, managing water supplies is becoming increasingly vital. Not only must storage and quality be considered, but also conveyance. In most developed countries, clean water can be brought into homes and buildings via extensive pipe networks. Likewise, wastewater tends to be brought to treatment facilities in separate pipe networks. However, in both developed and undeveloped countries, it is open-channels (Figure 1.1) that are heavily relied on to move water for agricultural irrigation, which is the largest use of fresh water in the world, making the movement of this water vital to the survival of billions of people. As a result, much work has gone into understanding open-channel flow and how to control it. Some of the major outcomes of this work are the development of a variety of hydraulic structures.

Figure 1.1 - Example Irrigation Canal (Takouleu 2020).

Much of the world relies heavily on the use of hydraulic structures to achieve adequate flow in open-channels. Some of the most popular of these structures are sharp-crested weirs and, more recently, pivot weirs. A sharp-crested weir (shown in Figure 1.2) is defined as an obstruction perpendicular to the flow direction whose crest (top over which the flow passes) is less than 2 mm in said flow direction. Acting almost as a low-level dam, the sharp-crested weir will back up the flow upstream before it passes over the obstruction. Similar to the sharp-crested weir, the pivot weir (Figure 1.3) is also a barrier that operates in a similar manner, except the weir is often inclined at an angle that can be altered as needed. The ability to change the inclination angle allows for greater flexibility in flow regulation. Both types of weirs are used extensively in open channels to regulate and/or measure flows.

Figure 1.2 - Example Sharp-Crested Weir (Wiktionary 2021).

Figure 1.3- Example Pivot Weir (Obermeyer Hydro, Inc 2021).

Extensive study of the sharp-crested weir has been conducted to better understand how it functions. Most notable of this work is the development of rating (head-discharge) equations which relate flow characteristics around the weir to flow over the weir (Horton 1907). Both the sharp-crested weir and pivot weir have derived rating equations that are commonly used to help operators control flow. However, a number of uncertainties remain when it comes to the application of sharp-crested weir rating equations for a wide variety of flow types. The limits of use for the classical rating equation have yet to be explored and the exact relationship between the discharge coefficient and head is unknown. Similarly, the behavior of flow over a pivot weir is still poorly understood. The understanding of how upstream head changes as the gate angle changes has never been done. By analyzing these areas of the weir, flow in open-channels can be better controlled and regulated in the field. This means better accuracy and more precise distribution of fresh water, leading to increased efficacy and equitability.

There are three main methods for studying hydraulic structures in open-channels: laboratory, field, and computational. Laboratory work uses smaller-scale flumes and lower flow rates. Field work examines existing full-scale structures in use. Computational work is growing as a favorite method for research studies in hydraulics due to the popularity of computational fluid dynamics (CFD). CFD is a combination of fluid mechanics, numerical methods, and computational code to simulate fluid flow under given conditions. Its versatility and imaging capabilities make it a useful tool in learning more about fluid flows, especially environmental flows (Bates et. al. 2005). The studies presented in this paper focus on using CFD as the main method for analyzing both types of weirs.

1.2 - Purpose

The purpose of this investigation was to use CFD to analyze in greater detail the behavior of flow over sharp-crested and pivot weirs in relation to regulation and measurement. For the sharp-crested weir, identification of an ideal-operating range for use of the classical rating equation was studied, as well as turbulent patterns upstream of the weir. Similarly, the pivot weir was analyzed to characterize flow conditions of a varying number of gate angles as affected by the upstream head. The work described in this thesis was entirely conducted with CFD using a commercial flow solver called FLOW-3D.

1.3 – Thesis Outline

There are five additional chapters in this thesis. The next chapter presents in-depth background information and a literature review on the sharp-crested weir, pivot weir, and CFD. Chapter 3 describes some preliminary studies conducted to identify best-practices in building hydraulic models of open-channel flow in FLOW-3D. The study of the sharp-crested weir is presented in Chapter 4 with the pivot weir study following in Chapter 5. A conclusion and expected future work are described in Chapter 6.

CHAPTER 2 – BACKGROUND AND LITERATURE REVIEW

2.1 - Sharp-Crested Weir

As mentioned previously, extensive work has gone into understanding the sharp-crested weir due to its popularity and simplicity. One of the most important discoveries to come out of these works is the development of the discharge equation. Due to its nature as a control structure, it was important to be able to relate known or measurable quantities of the flow to the flow rate in order to accurately control the fluid as desired. The first references to a discharge equation appear as early as 1907 in a USGS publication on experiments done with weirs by Robert Horton.

Derived from the Bernoulli equation, several assumptions had to be made to simplify the problem. First, it is assumed that the velocity distribution is developed and uniform prior to reaching the weir. Next, it is assumed that flow over the weir creates a well-formed nappe with atmospheric pressure underneath. Streamlines over the weir crest are also assumed to be horizontal which would make pressure within the nappe zero. Finally, it is given that the viscous effects in the flow are small enough to be considered negligible.

Utilizing all of these assumptions as well as integrating a form of the equation that works for a weir that spans the full width of the channel, the fully-contracted sharp-crested weir equation is obtained. It relates either the upstream elevation head (Equation 1) or total mechanical energy head (Equation 2) above the weir to the flow rate. Undergoing few changes over the years, the form of the equation presented will be from Tracy (1957) and Bos (1976). The original derivation of the equation, Equation 2, uses the total mechanical energy head (Equation 3), *H*, over the weir. However, measuring velocity head in an open-channel is often difficult without specialized equipment. Bos (1976) stated that the elevation head, h, typically makes up the majority of the total energy head and can be used in place of H.

$$Q = \frac{2}{3} C_d b \sqrt{2g} h^{3/2} \ldots \ldots \ldots \ldots \ldots \ldots \ldots \text{ Equation 1}$$

$$Q = \frac{2}{3} C_{dT} b \sqrt{2g} H^{3/2} \ldots \ldots \ldots \ldots \ldots \ldots \ldots \text{ Equation 2}$$

Where Q = volumetric flow rate,

b = width of the weir,

g = gravitational constant.,

C_d = discharge coefficient for Equation 1,

C_{dT} = discharge coefficient for Equation 2.

$$H = h + \frac{\bar{u}^2}{2g} \ldots \ldots \ldots \ldots \ldots \ldots \ldots \text{ Equation 3}$$

Where $\bar{u}$ = average cross-sectional velocity approaching the weir. All other terms are the same as those previously defined.

With the assumptions needed to derive Equations 1 and 2, a coefficient is introduced to account for the simplifications. C_d is a discharge coefficient that accounts for the assumptions as well as the missing approach velocity head. C_{dT} is a discharge coefficient that only accounts for the assumptions listed above. One of the most important issues with sharp-crested weirs is identifying the discharge coefficient. Typically, a curve is created to relate *H/P* or *h/P* to the respective discharge equations in order to have a variety of coefficient values. Oftentimes this is done after the weir has been installed in the field and data can be gathered to create such a curve. Similar processes can be done in experimental studies at model scale. In either case, the discharge coefficient is backed out from the discharge equation after obtaining an estimate for Q and either the H or h value.

Both h and H must be measured far enough upstream to avoid the acceleration region close to the weir. Typically, it is recommended that they be measured either 4 to 5 times the weir height upstream or 4 to 5 times the H or h value (Bos 1976). Important sharp-crested weir variables and zones are shown in Figure 2.1. The flow in Figure 3 is considered free-flow, where the downstream flow depth is below the weir height. Weir flow can also be submerged, where tailwater depth is also sufficiently above the weir height. Flow downstream of the weir then begins to have an effect on upstream flow, making the problem more complex. In field and experimental studies, additional equations or variables are introduced to account for this. However, only the free-flow condition will be depicted at this point in time.

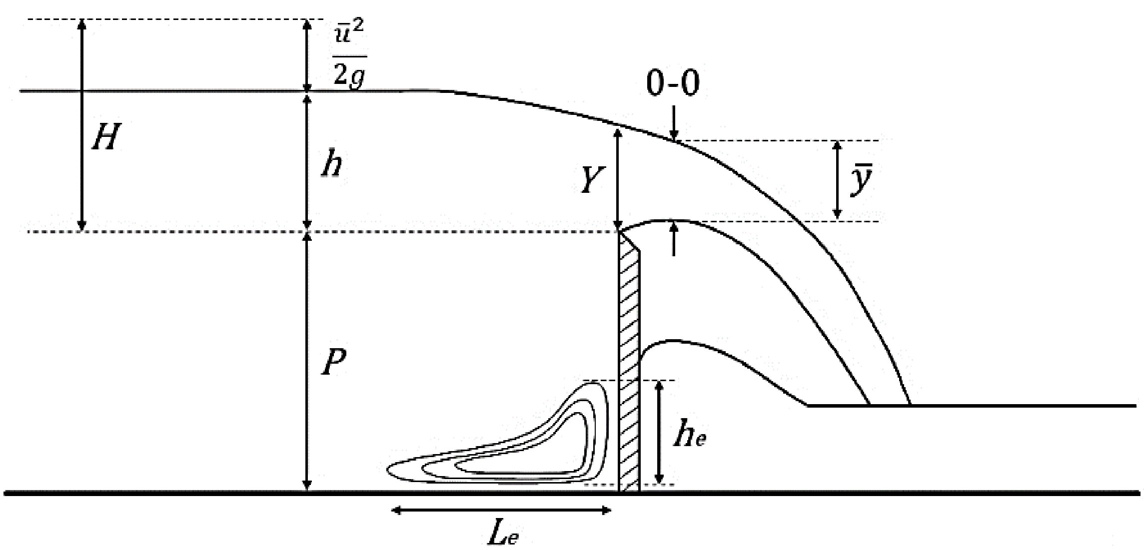

Figure 2.1 - Sharp-Crested Weir Diagram.

Where P = weir height, measuring from the base of the channel to the crest of the weir,

L_e = measured eddy length directly upstream of the weir. It is measure from the point where flow streamlines separate and gain an upward velocity vector to the weir,

h_e = height of the recirculation eddy upstream of the weir. It is measured from the bottom of the flume up to where the streamlines separate in between flowing over the weir and flowing back into the recirculation zone,

Y = depth directly above the crest,

$\bar{y}$ = thickness of the nappe at Section 0-0,

Section 0-0 = point where the bottom of the nappe is at its highest elevation, which correlates to the point with minimum energy head.

In cases of submerged flow, Villemonte (1947) proposed the introduction of a submerged flow factor by experimentally studying weir flows. The submergence factor relates the upstream and downstream depths above the weir to determine if flow is submerged. If the ratio of downstream to upstream elevation head exceeds a certain value, then said ratio is used in the calculation of a submergence coefficient. The coefficient is then multiplied into the discharge equation. Some models presented later are submerged flow, but the submergence factor and coefficient will not be introduced as submerged flow is not the focus of the following studies.

Given the difficulty in measuring flow rate or head values, other equations have been developed to estimate C_d. The most widely known of these was developed by Rehbock in 1929 and is aptly named the Rehbock Equation, presented in Equation 4. It predicts a linear relationship between the discharge coefficient, C_{dR}, and h/P.

$$C_{dR} = 0.611 + 0.075\frac{h}{P} \dots\dots\dots\dots\dots\dots\dots \text{Equation 4}$$

The coefficients obtained from this equation can be used with the form of the discharge equation presented in Equation 1. Henderson (1964) showed that estimates from the Rehbock Equation can only be used where pressure under the nappe is atmospheric. They also concluded that there was good agreement between C_{dR} and C_d for h/P values less than 5.

One of the other notable works was done by Kindsvater and Carter in 1959 where they reanalyzed the weir discharge equations in order to take viscosity and surface tension into account, two factors that are not accounted for due to the assumptions inherent to the Bernoulli equation. They derived an equation that was able to account for those effects. They also studied the coefficient of discharge and found it could be related to geometric ratios related to the weir itself as well as the channel.

A work by Rajaratnam and Muralidhar in 1971 focused on pressure and velocity distributions surrounding the weir. After conducting a number of experimental studies on the sharp-crested weir for a variety of h/P values, they analyzed the velocity and pressure distributions at the crest of the weir and at Section 0-0 (see Figure 3). They also conducted a small study to look at the eddy length upstream of the weir. One of the important discoveries that came about from their experiments was the identification of a collapsed curve when the non-dimensional velocity and pressure profiles are plotted on one another. Rajaratnam and Muralidhar also found that the eddy length continuously increased in value for $0 < h/P < 2$.

In Bos' 1976 book on Discharge Measurement Structures, he found that the velocity head tends to only make up a small fraction of the total energy head in most cases. Thus, the velocity distribution coefficient can generally be used as 1. He also derived discharge equations for the sharp-crested weir for varying channel geometries, such as parabolic or triangular.

Continuing from the Rajaratnam 1971 study, Ramamurthy et. al. (1987) also analyzed pressure and velocity distributions over a sharp-crested weir as well as relating the discharge coefficient to h/P for both free-flow over the weir as well as submerged and sill flow. In the end, they found that the discharge coefficient and h/P are related semi-empirically. Their pressure and velocity distributions also showed good agreement with those done by Rajaratnam and Muralidhar.

Swamee presented the discharge equations for the sharp-crested weir, broad crested weir, narrow-crested weir, and long-crested weir in 1988. He also provided a number of equations for estimating the discharge coefficient for each of these weirs before compiling them into a single equation. Swamee validated these findings by comparing the theoretical results to experimental results. He concluded that his proposed coefficient equation could hold for extreme head to weir height and head to weir width ratios.

In 2000, Michael Johnson studied flow over flat-topped and sharp-crested weirs to help provide engineers with a way to better estimate the discharge coefficient. Looking at a wide variety of flow rates for multiple weirs, he plotted the discharge coefficient against H/P for the flat-topped weirs. In addition to providing guidelines for engineers to use the data he obtained, Johnson found the lack of a linear relationship between C_{dT} and H/P.

Qu et. al. (2009), working with Ramamurthy, used CFD to recreate Ramamurthy's 1987 experiments on sharp-created weir flows. They utilized 2D equations with a volume of fluid (VOF) method and k-ε turbulence model to validate CFD with experimental studies. Qu et. al. were able to state the ability to accurately recreate experimental studies with low error, meaning CFD was a viable option for adding further insight to sharp-crested weir problems.

Also in 2009, Bagheri and Heidarpour experimentally studied the nappe structure over a sharp-crested weir. They found that the lower and upper nappe profile could be fitted to second- and third-order polynomial functions. Bagheri and Heidarpour (2009) also calculated the discharge coefficient using a free-vortex theory and found it agreed well with past coefficient calculations.

Angela Ferrari used a newer numerical modeling tool called Smoothed Particle Hydrodynamics, or SPH, to simulate flow over a sharp-crested weir in 2010. The purpose was to identify if SPH could be used for flows such as these and to validate numerical analysis with experimental data. In the end, Ferrari found that SPH could be used to simulate flow over sharp-crested weirs, including the more complex aspects of flow impact and swirling. The meshless approach proved to be beneficial in making up for the other additional costs of using SPH.

In 2011, Rady conducted both 2D and 3D models of flow over sharp-crested weirs in FLOW-3D. He looked at the discharge coefficient as well as contours and vectors surrounding the weir. Rady also stated that in order to follow best-practices and produce accurate results, the velocity head should not be neglected in flow calculations over the weir. He created a series of steps for engineers to follow to best use both the weir discharge equation as well as selecting a discharge coefficient.

Further CFD studies were done by Mahtabi and Arvanaghi in 2018 using a commercial code called ANSYS Fluent. After altering the h/P value and calculating the discharge coefficient, they found that C_d decreased nonlinearly for $Re < 20,000$. The coefficient then became constant with a value of 0.7 for $Re > 20,000$ which corresponds to $h/P > 0.6$. Mahtabi and Arvanaghi conducted these tests on 3 separate weir heights and found similar results.

2.2 - Pivot Weir

A relatively newer hydraulic design, the pivot weir aims to provide more flexibility in flow control. While the sharp-crested weir is stuck at a constant height perpendicular to the channel bed, the pivot weir can incline itself to either lower or raise the effective height, changing its influence on flow in the channel. The pivot weir still behaves similarly to the sharp-crested weir, with an almost identical discharge equation, shown in Equation 5, which was derived by Wahlin and Replogle (1994). The major difference in the pivot weir equation is the introduction of a second coefficient. While the sharp-crested weir equation has a single coefficient dependent on the head above the weir, the pivot weir equation requires a second coefficient, C_a, to account for the weir angle.

$$Q = \frac{2}{3} C_d C_a b \sqrt{2g} h^{3/2} \ldots\ldots\ldots\ldots\ldots\ldots\ldots \text{Equation 5}$$

Each of the other variables is the same as those already defined. Also, similar to the sharp-crested weir, an alternate equation can be formed using the total mechanical energy head as opposed to the total elevation head. The two distinct discharge coefficients can also be combined to form a single discharge coefficient, making the pivot weir equation the same as Equation 1.

A general diagram of the important weir variables is depicted in Figure 2.2. Of particular note is the new variable for weir length, *L*. The weir height, *P*, is still measured as the vertical distance from the channel bed to the weir crest. Therefore, it is a dependent variable on the weir angle, θ. Weir length remains constant in each trial, regardless of angle. In addition to the calculated or studied variables, an important note of turbulent structures surrounding the weir can be made. In the sharp-crested weir, the recirculation zone only appeared upstream of the weir, where flow could not easily navigate vertically over the weir. In the pivot weir, the large recirculation zone can appear either upstream or downstream depending on the inclination angle. In low angles, the recirculation zone only appears downstream under the weir because the flow can easily maneuver over the weir, but can sometimes become trapped under it on the downstream side. The turbulent zone appears on either side of the weir in angles close to 90°, but usually greater than 60°.

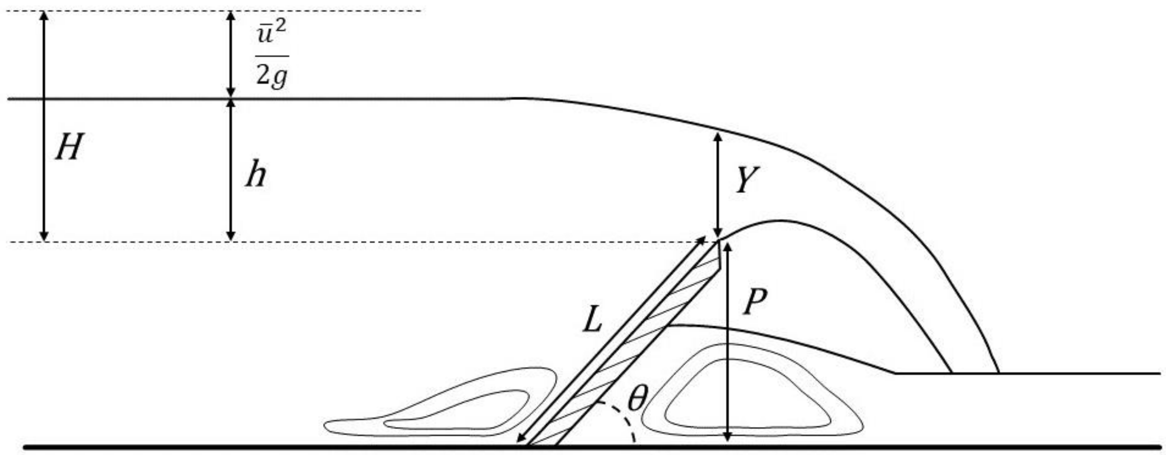

Figure 2.2 - Pivot Weir Diagram.

Wahlin and Replogle (1994) conducted a series of experimental trials on overshot gates for six different angles: 90.00°, 71.57°, 56.31°, 45.00°, 26.57°, and 14.04°. They concluded that, at high angles, the weir functioned like a sharp-crested weir still, while at lower angles the flow looked more like a free overfall. Wahlin and Replogle also found that, as the angle of inclination decreased to 45°, the vena contracta thickness increases. However, after 45°, the vena contracta thickness begins to decrease.

Prakash et al. (2011) developed a discharge-head equation for an inclined rectangular weir. It was found that increasing the inclination angle increases the discharge capacity of the weir. The head-discharge equations were found to be power laws with a unique coefficient for each inclination angle.

In 2017, Azimfar et al looked at the derivation of the discharge coefficient for a pivot weir under both free and submerged flow. They proposed several equations as a means to estimate the discharge coefficient under a wide range of flows that were derived from the momentum equations and Bernoulli equation.

Experimental and numerical simulations of inclined rectangular weirs were done by Bijankhan and Ferro (2018). The purpose of this was to explore how the angle of inclination would change the discharge equation. To do so, a flow magnification ratio was defined as the discharge through the pivot weir divided by the corresponding discharge over a vertical sharp-crested weir. The ratio increased as angle decreases until the maximum value at 30°, the lowest angle tested in this study. Bijankhan and Ferro (2018) obtained similar results using 3D models using the OpenFOAM CFD code.

Bijankhan and Ferro also conducted numerous studies on pivot weirs in 2020 to specifically identify what factors affected submergence. They studied weirs with inclinations angles of 39.6°, 53°, 85°, and 90° with a number of different flow rates. Using dimensional analysis, an equation was derived to differentiate between the free and submerged conditions. Experimental results were then used to calibrate this equation.

SPH analysis, a numerical technique discussed previously, was used by Mahdavi and Shahkarami in 2020 to analyze the free surface of flows over the pivot weir. Five different angles, 90°, 60°, 45°, 26.57°, and 14.04°, were modeled for a number of flow rates. Validation of the models was done with previous experimental results. The vena contracta was observed to shift further downstream with an increase in inclination angle.

One particular note of importance is a discussion on a particular type of pivot weir called the Obermeyer weir (Obermeyer 2018). Commonly used in irrigation canals, the Obermeyer weir has several design features useful in understanding the workings of a pivot weir. First, the gate angle is controlled by an air bladder that sits under the gate. Air can be pumped into or out of the bladder to raise or lower the gate, with the pressure inside the bladder maintaining the angle. The gate itself is usually curved to help flow navigate itself over the weir more efficiently. The Obermeyer weir is the subject of study in the related experimental work in the Environmental Fluid Mechanics Laboratory (EFML) and inspired the design of the lab model. It is worth mentioning that the weirs studied in this study will be inclined sharp-crested weirs, without the curve in weir structure.

2.3 - Computational Fluid Dynamics

With advancements in computing power, speed, and versatility, a method of computationally simulating fluid flow was created in the 1960s. Computational fluid dynamics, or CFD, combines numerical methods, computational tools, and fluid mechanics to model fluid flow for any number of situations. Almost all commercial and research CFD codes have the same 3 stages of developing a model: pre-processing, solver, and post-processing (Versteeg and Malalasekera 2007). In the following section of the paper, a model will be defined as the code and conditions built for a specific CFD problem. A simulation is a single run of the already built model. Simulation of the same model can vary depending on the numerical approximations used, so it is important that this distinction be made.

2.3.1 - Pre-Processing

The pre-processing step includes understanding the problem to be modeled and determining the best computational approximations for creating a model. The domain, or solution space, must be defined along with any important geometries. In a case such as the study conducted in this paper, the domain would be the open-channel surrounding the weir. Any weir geometries would need to be built in AutoCAD or SolidWorks and exported as a .stl file.

Yet another pre-processing step is determining the physics that govern the fluid problem. The governing equations must be modified or added on to in order to account for gravitational, non-inertial, compressible, stratified, or any other effects. Furthermore, fluid properties must be determined. For most hydraulic CFD problems, water at 20°C is used in models. However, any number of fluids can be specified so long as the properties of said fluid can be given.

Once the domain, geometries, and physics are decided, typical CFD codes will require a computational mesh. The mesh is where the governing fluid equations will be solved or approximated. Smaller cells within the mesh typically increases the accuracy at the cost of computational time. A mesh can be either structured or unstructured, depending on the code. A structured code has a consistent cell size within a mesh block where each of the cells is a rectangular shape. In an unstructured mesh, cells can be triangles, hexagons, rectangles, or a number of other shapes that vary in size within the same block. Structured meshes are typically easier to create, but at the cost of resolving the geometry and difficulty in obtaining accuracy in some areas. Although difficult to create, an unstructured mesh will provide more flexibility in resolving complex geometries while also maintaining accuracy where needed.

Along with creating the mesh, boundary conditions must be specified. Boundary conditions take place at mesh faces to give the model enough information on how to run the model. For example, one mesh face might act as an inlet where the fluid will enter the domain. The model must know how and what amount of fluid will enter in order to properly run the simulation. Other examples of boundary conditions include walls, outlets, inflows, pressure conditions, and symmetry conditions. At wall conditions, the no-slip law will be enforced and, depending on the code, a roughness height can also be input to simulate additional frictional effects. Outlets typically allow fluid to exit the model domain with no normal-flux return of fluid. Inflow conditions are usually either volumetric flow rates or velocities. In either case, the condition is to allow fluid to enter a domain given a certain type of flow. A pressure condition is often used to simulate a reservoir of fluid or to prescribe depths at mesh faces that the simulation must attempt to reach. Symmetry conditions are used when a problem can be simplified using a symmetry assumption, but they can also be used in other instances. A symmetry condition implies a zero-gradient as well as a zero normal velocity flux condition at the symmetry plane. There are numerous other boundary conditions, but these are the ones primarily used in the following studies.

2.3.2 - Solver

The governing equations that describe fluid motion and physics are almost always too difficult to solve analytically. They are usually made of different partial differential equations that can be coupled or are comprised of different types of derivatives. In order to actually solve these equations, they are discretized to be solved numerically. There are 3 popular solution methods for CFD solvers: finite difference, finite element, and spectral methods. Each has its own advantages and disadvantages, but the finite difference method will be the method of choice for the following studies. Specifically a type of finite difference method called finite volume method will be discussed.

In the finite volume method, the governing equations are solved such that scalar properties are solved at cell centers and vector quantities are solved at cell faces. Generally, the finite volume method will solve for a fluid or flow property based on its change in time, inflow and outflows, as well as any creation or dissipation within the cell. The discretized governing equations are integrated into each cell within the mesh before being solved iteratively through various methods. Depending on the code and problem, different levels of accuracy as well as the type of discretization may be used. As a result of this, special care must be taken with the spatial and time steps so as to obtain convergence and accurate solutions. Codes can either continuously alter the time step to find the best-suited value, or will allow for user input.

2.3.3 - Post-Processing

With the completion of a simulation, data must be extracted and processed. Depending on the code used, a commercial post-processing software may be used for easier data manipulation. Velocity, pressure, and other scalar and vector quantities can all be checked for accuracy or to make calculations. Typically, contour plots of flow characteristics are made for visuals of flow that normally would not be possible with lab or field equipment. Streamlines and pathlines can also be created to visually show how the fluid moves or will move. In this final stage, additional accuracy and sanity checks are also made to ensure the model was constructed correctly and is operating without issue.

2.3.4 - Governing Theory of a CFD Code

The underlying equations for almost all CFD simulations are the Navier-Stokes Equations, Equation 6, along with the Continuity Equation, Equation 7. The Navier-Stokes Equations are originally derived from Newton's Second Law and are a modified form of the conservation of momentum equation. Fluids cannot be solved in the same way as a discrete object, so most conservation equations undergo a transformation from a Lagrangian approach to an Eulerian approach using the Reynolds Transport Theorem.

With Equations 6 and 7, a fluid flow can be approximated. As they are presented below, these equations are for incompressible flow as in an inertial frame of reference. Almost all hydraulic engineering flow simulations utilize these simplifications.

$$\frac{D\boldsymbol{U}}{Dt} = -\frac{1}{\rho}\nabla p + \nu\nabla^2\boldsymbol{U} \dots \dots \dots \dots \dots \dots \dots \text{ Equation 6}$$

$$\nabla \cdot \boldsymbol{U} = 0 \dots \dots \dots \dots \dots \dots \dots \text{ Equation 7}$$

Where U = velocity vector,

ρ = fluid density,

p = the pressure,

ν = kinematic viscosity.

For problems that also have gravitational effects, porous media, or any other additional physics, extra terms may be added to either equation to account for those. However, the Navier-Stokes equations are a highly complex mix of elliptical (pressure term), parabolic (viscous term), and hyperbolic terms (acceleration).

It is impossible to directly solve this set of partial differential equations directly, so numerical methods are used. The governing equations are made into a system of algebraic equations which can then be solved iteratively. The same numerical approximations were used for each simulation in this study. For the momentum-advection terms, a first-order accurate upwind scheme was implemented and for the pressure terms a generalized minimum residual algorithm (GMRES) from Saad (1986) was used. The solution was also marched in time with a first-order scheme. The first-order accuracy was chosen over second-order due to the lack of need for the additional accuracy and computational cost. After validation, the first-order accuracy models were already adequately matching experimental results, so the additional computational costs associated with second-order accuracy were not justified. The GMRES method is highly accurate and can be used for a wide range of problems (FLOW-3D 2019). Its ability to easily converge make it useful for a parametric study where a number of simulations must be run in a short time.

2.3.5 - Turbulence Models

Many practical fluid flow problems must also consider the issue of turbulence. Turbulence is a state of flow characterized by randomness, nonlinearity, dissipation, vorticity, and diffusivity. Its complexity makes it extremely difficult to completely recreate in a computational model and its susceptibility to minute changes means recreating experimental results exactly is impossible. However, a great deal of work has gone into working with turbulence in CFD models. Three major methods of dealing with turbulence generally used are: Direct Numerical Simulations (DNS), Large Eddy Simulations (LES), and Reynolds-Averaged Navier-Stokes (RANS) Models.

In a DNS simulation, turbulence is solved for directly with the Navier-Stokes equations. The smallest scales of turbulence, the Kolmogorov Scales, are solved without approximations or other methods of simplification. Because of this it can produce highly accurate results for modeling turbulence and is considered the highest standard for making realistic simulations. However, DNS has some extreme drawbacks that greatly limit its use. First, in order to model all scales of turbulence, the computational mesh must be fine enough to capture the smallest vortices. This typically is on the order of hundredths of a millimeter, meaning even a small-scale problem could have upwards of a billion cells. Increasing cell count leads to exponential increases in computational time and power required. It takes specialized computers with high processing power to run DNS. Furthermore, because of the complexity of turbulence, DNS cannot be used for many practical problems. Simulating a sharp-crested weir for example would introduce too many other variables for the model to keep up. As such, DNS is typically limited to very simple problems, like flow over a flat plate or an extremely simple open channel flow.

With DNS being so limiting, other methods that involve modeling some scales or turbulence were discovered. A popular research method is using an LES model which compromises between computational costs and accuracy in CFD models. In an LES model, a spatial filter is applied where larger scales of turbulence are solved directly and small scales are models. The size of the filter is dependent on the resolution of the grid, i.e finer resolution means more eddies will be directly solved for. The LES model was not selected for use due to its additional computational costs and the additional information provided by LES was not necessary. LES models are powerful when flow variable fluctuations with time are important. However, for this study, time-averaged quantities were adequate, leading to the selection of the RANS turbulence model, which will be discussed in the following paragraphs.

The final method of dealing with turbulence in CFD are RANS models. They are the least computationally costly and are the most widely used turbulence models. RANS is an encompassing term where there are several distinct models under the umbrella term. However, they all have many similar characteristics. While the LES models apply a spatial filter, RANS models use a time filter. The first step in adjusting the Navier-Stokes Equations to include this time filter is applying a Reynold's Decomposition, seen in Equation 8. Reynold's Decomposition breaks an instantaneous quantity into a fluctuation added to an average value. It can be applied to any measured quantity, such as velocity or pressure.

$$X = \langle X \rangle + x \ldots \ldots \ldots \ldots \ldots \ldots \ldots \text{ Equation 8}$$

Where X = instantaneous variable,

$\langle X \rangle$ = average variable,

x = fluctuating variable.

The decomposition is then substituted into the Navier-Stokes Equations for each variable and simplified to cancel terms out. What is left is largely the same equations with time-averaged values instead of instantaneous ones with the new equations called the Reynolds equations, Equation 9. However, there is one major difference in the appearance of the Reynolds Stresses, the final term on the right-hand-side in the time-average equations.

$$\frac{\bar{D}\langle U_j \rangle}{\bar{D}t} = -\frac{1}{\rho}\frac{\partial \langle p \rangle}{\partial x_j} + \nu \nabla^2 \langle U_j \rangle - \frac{\partial \langle u_i u_j \rangle}{\partial x_i} \ldots \ldots \ldots \ldots \ldots \ldots \ldots \text{ Equation 9}$$

Each of the variables is the same as those already presented, but terms in brackets are averaged quantities. The lowercase variables in the final term on the right-hand-side are fluctuating terms.

The Reynolds Equations with the averaged Continuity Equation have four total equations but more than four unknowns, resulting in the closure problem. Additional equations are needed to solve for the Reynolds stresses if the time averaged equations are to be used. One important aspect of the Reynolds stresses is the turbulent-viscosity hypothesis which states that the deviatoric Reynolds stress is proportional to the mean rate of strain. This hypothesis provides a way to solve for the Reynolds stresses so long as a turbulent, or eddy, viscosity, ν_T, can be specified. The turbulent viscosity is often modeled as a velocity term multiplied by a length term. The distinct models under the RANS umbrella will use different equations or different numbers of equations to determine this velocity and length term.

The specific model that will be discussed in this paper is the RNG k-ε model, arguably the most popular turbulence model. The RNG k-ε model solves for two additional variables: turbulent kinetic energy, k, and rate of turbulent kinetic energy dissipation, ε. The two additional variables are then related to the velocity and length terms required to solve for the turbulent viscosity. Using the turbulent viscosity, the Reynolds stresses can be solved and the closure problem mended. Although it was created through physical reasoning, experimental analysis, and dimensional analysis (Sotiropoulos 2005), it can accurately model flow far from walls. There are several coefficients that need to be used to completely close the model. The RNG method uses the Renormalization Group method to calculate these coefficients. The RNG k-ε model has been extensively used and validated for all manner of simulations. It excels in simple flows (Pope 2000), such as 2D flow over a weir.

2.3.6 - FLOW-3D as a Computational Tool

As has been mentioned previously in this paper, a specific commercial code called FLOW-3D which was developed by Flow Science Inc. will be used in the studies conducted for this project. It generally uses the theory and methods talked about earlier, but with some distinguishing features that make it better suited to hydraulic flow modeling.

The most notable difference between FLOW-3D and other commercial solvers is its method for solving for the free surface. FLOW-3D uses a unique algorithm called the Volume of Fluid (VoF) method (Hirt and Nichols 1981) which will track the free surface as it moves from cell to cell. A variable F is defined as the fraction of the cell that contains the fluid. A value of 1 means the cell is full of fluid while a value of 0 means the cell has no fluid. Therefore, the free surface is where F is between 0 and 1. An equation, Equation 10, can then be written for F to track and alter the free surface as it moves through the model space.

$$\frac{\partial F}{\partial t} + \frac{1}{V_F}\left[\frac{\partial u}{\partial x}(FA_x u) + \frac{\partial u}{\partial x}\left(FA_y v\right) + \frac{\partial u}{\partial x}(FA_z w)\right] = 0 \ldots\ldots\ldots\ldots\ldots\ldots\ldots \text{ Equation 10}$$

Where V_F = fluid volume fraction (fractional volume open to flow),

A_x = fractional area open to flow in the x direction,

A_y = fractional area open to flow in the y direction,

A_z = fractional area open to flow in the z direction,

u, v, and w = velocities in the x-, y-, and z-directions respectively.

In terms of meshing, FLOW-3D uses a completely orthogonal grid where each cell is a rectangular prism or cube. A method such as this makes mesh creation simple and a single mesh can be used for a number of geometries. However, additional code must be written to integrate the geometry within the mesh. FLOW-3D uses a specific algorithm called the Fractional Area/Volume Obstacle Representation, or FAVOR. FAVOR will analyze the area and volume fractions of a geometry that lie within a cell in the mesh. For a geometry to be realizable within a cell, it must contain at least one corner of said cell. If the geometry contains all four corners of the cell, then it will be completely resolved within the cell. An example of this process is seen in Figure 2.3, where the original geometries appear on the left and the FAVOR resolved geometry on the right. FLOW-3D introduces several terms into the Navier-Stokes equations for the solver in order to account for the FAVOR method.

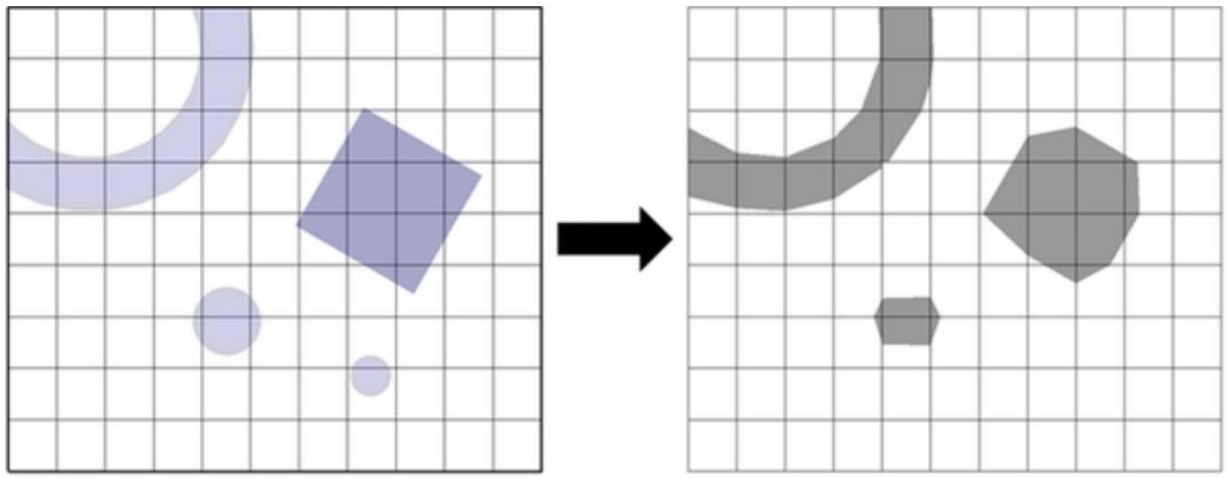

Figure 2.3 - FAVOR Resolution for FLOW-3D Mesh (FLOW-3D 2021).

To achieve better geometry resolution, a finer mesh is often needed. This can mean reducing cell size for the entire mesh or using a nested mesh. A nested mesh is a more resolved mesh block that lies within an outer mesh. It typically will only cover an area where geometry needs to be resolved or where more data is desired. For the following studies, nested mesh was typically used to better resolve the weir geometry and get rid of any holes that might have occurred without it.

An example of FAVOR and the meshing tactics discussed for the pivot weir models can be seen in Figure 2.4. The cells are all rectangular with a finer nested mesh over the weir region, seen in the top image. The image in the middle geometry as given to FLOW-3D from SolidWorks. The last image is what the simulation will see after FAVOR has calculated the ratios and built the geometry within the mesh. It can be seen that FAVOR is not able to completely recreate the geometry. The weir has a small fraction missing from the crest and adopts a step shape due to the inability of FAVOR to create smooth surfaces without adequate cells. However, the geometry built by FAVOR is a close approximation and suitable for the simulations. The exact weir heights were measured and recorded to account for any issues in resolution.

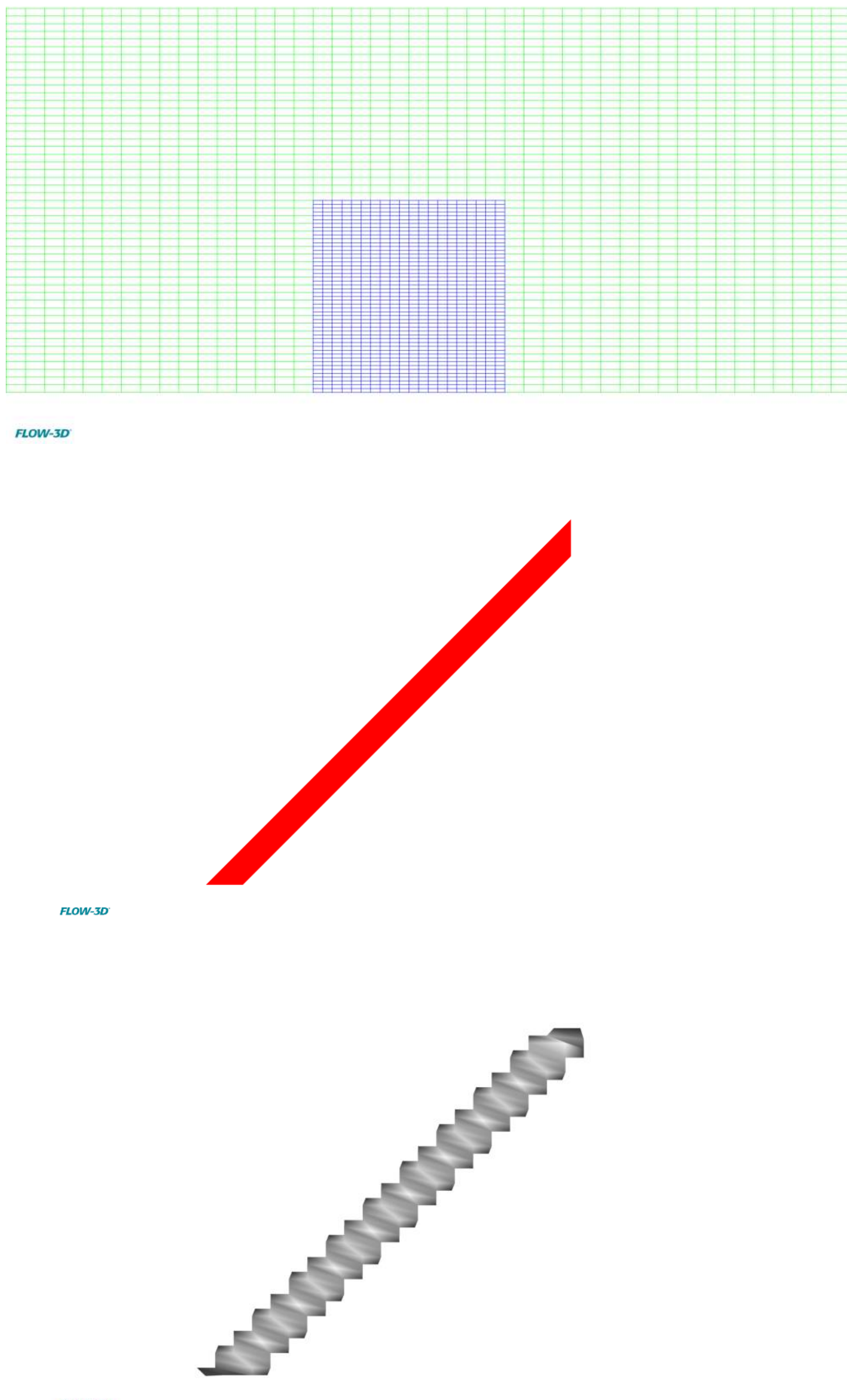

Figure 2.4 - Mesh and Geometry Images for 47° Pivot Weir in FLOW-3D.

FLOW-3D has been extensively validated through many internal and external studies for a variety of fluid problems. Milano (2013) validated the VoF method for fluid in a container. A rectangular container with a 3D model subject to fluctuations was made. Computational results were compared to analytical expectations, showing good agreement between the two.

An in-house validation conducted by FLOW-3D studied flow over piano weirs. Based on an experimental study conducted by Anderson (2011), a model was created to simulate flow over the weir in 3D using a number of different resolutions. The results from the model showed good agreement, with less than 5% error in head over the weir between the computational and experimental models. It was also found that, to best resolve the weir geometry, cells were recommended to be smaller than the width of the weir.

In 2016, Bayon et. al. compared CFD results between FLOW-3D and another popular open source code OpenFOAM. A hydraulic jump at low Reynolds number was studied and compared to existing experimental results. Bayon et. al. found that FLOW-3D exceled at modeling the interaction between the super- and subcritical depths, as well as a higher level of accuracy in the derived variables from hydraulic jump equations. OpenFOAM was better in recreating the overall structure of the jump.

2.4 – Dimensional Analysis

Prior to any study, an important step is to conduct a dimensional analysis to identify what variables might be important to analyze. Furthermore, it can eliminate variables that might not be necessary and prevent overcomplicating the study. The specific dimensional analysis that will be used here is the Buckingham-Π Theorem. This method will create non-dimensional groups from known variables. A number of variables, n, specific to the problem can be defined which are made up of a number of independent variables, *r*. The independent variables are typically, length, time, mass, or temperature terms. (*n* - *r*) dimensionless parameters are then defined, referred to as Π-groups.

For the sharp crested weir, 7 study variables were determined, shown in Equation 11. For the purpose of this study, only elevation head above the weir, *h*, will be analyzed. However, both elevation head and total mechanical energy head above the weir have the same units, so the dimensional analysis would be identical, but with *H* for total mechanical energy head above the weir instead of *h*, the elevation head above the weir. Also, dynamic viscosity, μ, is used here, but it can be substituted for kinematic viscosity.

$$q = f(h, P, g, \mu, \rho, \sigma) \dots \dots \dots \dots \dots \dots \dots \text{ Equation 11}$$

Where q = flow intensity (flow rate per unit width)

σ = surface tension

In the 6 study variables, there are three independent variables. Therefore, 4 dimensionless Π-groups were made with h, q, and ρ used as scaling variables. The final forms of the Π-groups are given in Equations 12 through 15.

$$\Pi_1 = \frac{q}{h^{\frac{3}{2}} g^{\frac{1}{2}}} \dots \dots \dots \dots \dots \dots \dots \text{ Equation 12}$$

$$\Pi_2 = \frac{h}{P} \dots \dots \dots \dots \dots \dots \dots \text{ Equation 13}$$

$$\Pi_3 = \frac{\rho g h^2}{\sigma} = We \dots \dots \dots \dots \dots \dots \dots \text{ Equation 14}$$

$$\Pi_4 = \frac{\rho g^{\frac{1}{2}} h^{\frac{3}{2}}}{\mu} = Re \dots \dots \dots \dots \dots \dots \dots \text{ Equation 15}$$

Therefore, the flow rate over the weir is dependent on three factors: the head above the weir, Reynolds number, and Weber number, *We*. The final form of the dimensional analysis is presented in Equation 16.

$$\frac{q}{h^{\frac{3}{2}}g^{\frac{1}{2}}} = \varphi\left(\frac{h}{P}, Re, We\right) \dots \dots \dots \dots \dots \dots \dots \text{ Equation 16}$$

The first Π-term is indicative of the discharge coefficient. Typically, as Reynolds number grows, the influence of the Weber number should decrease and surface tension and viscous effects become negligible. A similar dimensional analysis can be made for the pivot weir. Here, an additional term to account for the inclination angle must be introduced. A simplification for *P* can be introduced using the length and angle of the weir, shown in Equation 17.

$$P = L\sin(\theta) \dots \dots \dots \dots \dots \dots \dots \text{ Equation 17}$$

Therefore, the final form of the dimensional analysis is altered to that in Equation 18. It is largely the same, but the weir angle and length are now important factors in determining the discharge over a pivot weir.

$$\frac{q}{h^{\frac{3}{2}}g^{\frac{1}{2}}} = \varphi\left(\frac{h}{L\sin(\theta)}, Re, We\right) \dots \dots \dots \dots \dots \dots \dots \text{ Equation 18}$$

The results of both dimensional analyses provide information on the important variables for study. This is especially helpful in the parametric studies, where typically only a select number of variables are altered to identify their effects.

CHAPTER 3 – INITIAL STUDIES FOR PROPER USE OF FLOW-3D IN OPEN-CHANNEL HYDRAULIC MODELING

3.1 – Simulated Flow Development

Prior to beginning the CFD parametric studies, there were several additional studies that had to be done to determine the best practices in constructing CFD models of open-channel flow and hydraulic structures. The first was analyzing flow development in FLOW-3D. Unlike other commercial CFD codes, FLOW-3D provides no method for specifying a fully-developed velocity profile as fluid enters the model domain. Fully-developed, in this case, is where the velocity profile remains unchanged after some distance. Therefore, it was important to simulate the flow within the model itself. Using the volumetric flow rate boundary condition, the easiest method for allowing flow to develop was to extend the distance upstream of the active region of study.

To test the flow development capabilities of FLOW-3D, a 2D 10 m-long empty flume model was built with a specified flow rate. With a fluid fraction volumetric inflow boundary condition and an outflow boundary condition, the simulated flow developed into a supercritical state. However, after using the natural subcritical flow volumetric inlet, a specified pressure depth outlet condition, or a combination of the two, simulated flow was able to develop into a subcritical state. The simulated subcritical and supercritical flow depths are likely alternate depths. It was concluded that, without additional guidance, the open-channel flow simulations would converge on the supercritical state. Therefore, in cases where there was no weir to act as a downstream control or the weir's influence on flow was diminished, a change in boundary conditions was required to provide the model with adequate information to result in a subcritical flow simulation.

After analyzing the development of the different modeled states of flow, the simulated velocity profiles were analyzed for the subcritical flows. Velocity profile plots at several distances downstream from the upstream inlet are plotted in Figure 3.1. It can be seen that it takes several meters for the flow to achieve a fully-developed profile. Even 1.5 m to 6 m from the upstream inlet, the flow is far from developed. It is not until about 8 m downstream that the velocity profile can be considered developed with minimal changes over a 1 m span and has the characteristic turbulent boundary layer profile. The consequences of this finding is that the model domain must be expanded for flow development. The length was increased depending on the scale of the problem, from 4m to 15m. Additional checks were done on each simulation to make sure that flow development was simulated prior to reaching the study region. For the weir studies, careful attention also had to be paid to making sure flow developed prior to reaching the acceleration zone near the weir. The extended distances upstream of the weir will be discussed in further detail later in this thesis.

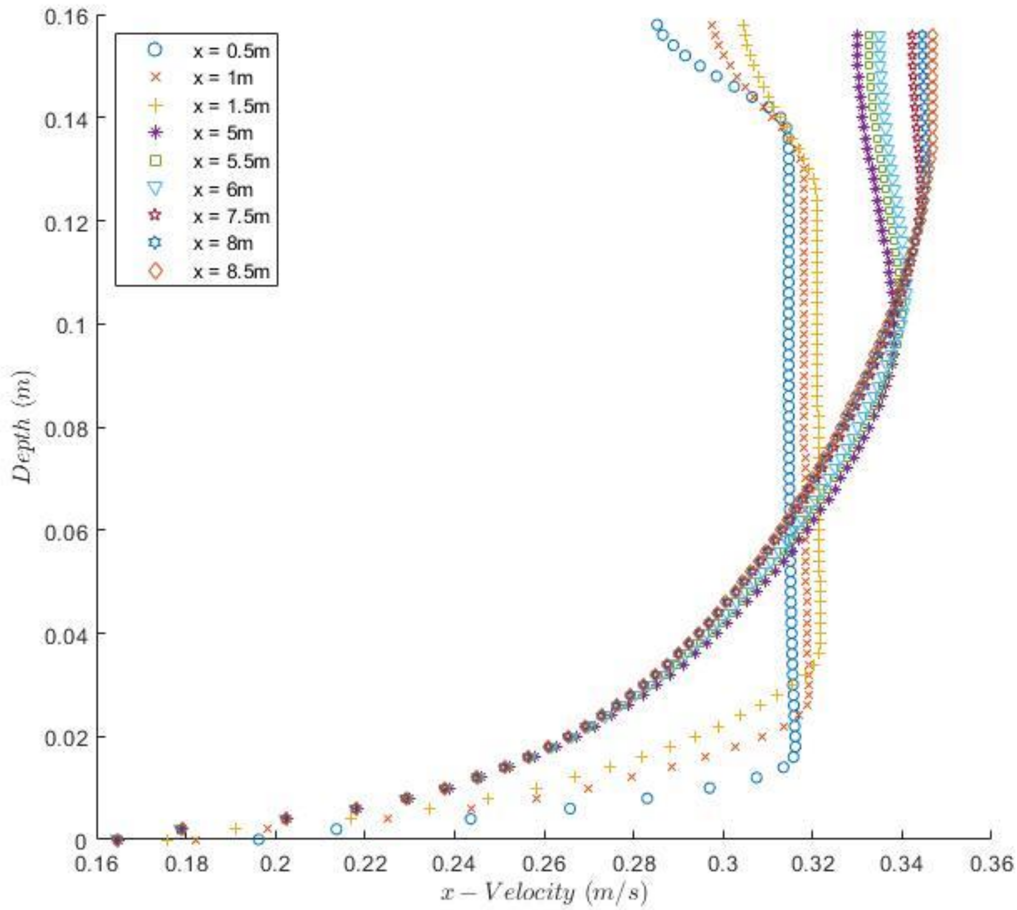

Figure 3.1 - Velocity Profile Development in an Open-Channel Flow CFD Simulation.

In addition to the simulations focusing on fully-developed flow, several simulations were run to test FLOW-3D's ability to develop a velocity profile extending from the bottom of the flume to the free surface. The velocity calculation in the first cell is carried out using the logarithmic law of the wall (log-law) boundary condition. The boundary region is highly active and extremely difficult to solve without simplifying assumptions. Using the log law to approximate the velocity in the first cell closest to the wall is well-validated. However, there are additional details regarding mesh resolution must be considered. FLOW-3D recommends that the y^+ (non-dimensional wall unit) value of the first cell lies within the log-law region, typically between a value of 30 and 100 to 500 depending on the model, shown in Figure 3.2. The y^+ value is a non-dimensional unit that is based on the local cell's velocity. It is an important term for turbulence and can generally be used to determine how fine or coarse a mesh is. Unfortunately, the y^+ value cannot be determined until after the simulation is run; thus having a general idea for an optimal resolution can greatly simplify model troubleshooting.

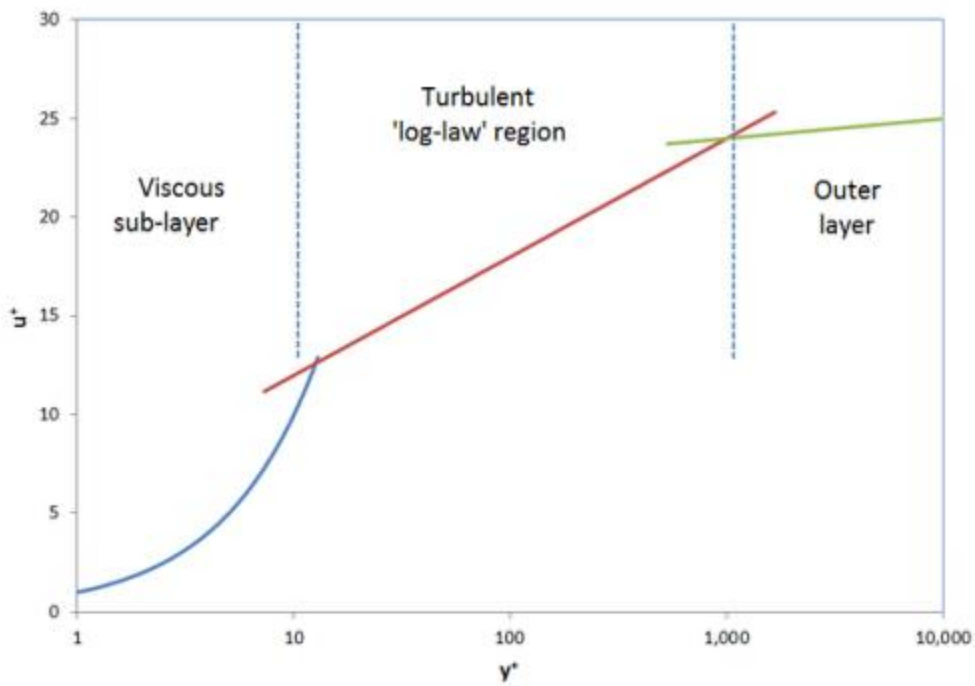

Figure 3.2 - y+ Regions in CFD simulations (FLOW-3D 2021).

Five 2D simulation were run where the first cell height was varied while all other variables and setup parameters were held constant. The model space was a 20 m long flume with a prescribed upstream and downstream depth of 11 cm to develop a subcritical flow, similar to conditions that would be seen upstream of a weir. The resulting simulated value of *Re* for each flow was roughly 66,000, which is a sufficiently turbulent open-channel flow. The grid cell resolution in the x-direction was 5 mm and, other than the first cell adjacent to the flume bottom, the y-direction (wall normal) resolution was 2 mm. First cell heights of 2 mm, 5 mm, 1 cm, 1.5 cm, and 3 cm were tested. Figure 3.3 shows the velocity profiles at a point where the simulated flow has had sufficient time to develop. Connecting lines were used with the markers in Figure 3.3 to better show the calculated velocity profile for each simulation.

The corresponding y^+ values for each first cell height were 28, 70, 140, 210, and 423. As the y^+ value increases, the velocity profiles tend to decrease in magnitude. However, this decrease is extremely small and only noticeably with large changes in y^+. The first velocity calculation increases in magnitude with an increased y^+ value which causes significant issues in the lower region of the profile. High first cell velocity calculations create unexpected “kinks” resulting in a profile that does not retain the smooth variation that would be expected within the turbulent boundary layer. It was concluded that, for the scale and types of flows tested in the FLOW-3D parametric studies, a first cell height of around 2 mm would be ideal, as it results in a realistically simulated turbulent boundary layer shape. Although on the lowest end of the recommended y^+ values, the 2 mm first cell height lies well enough outside the viscous sublayer to avoid additional errors. Each simulation had the first the y^+ value in the first cell calculated to make sure it was within the expected range.

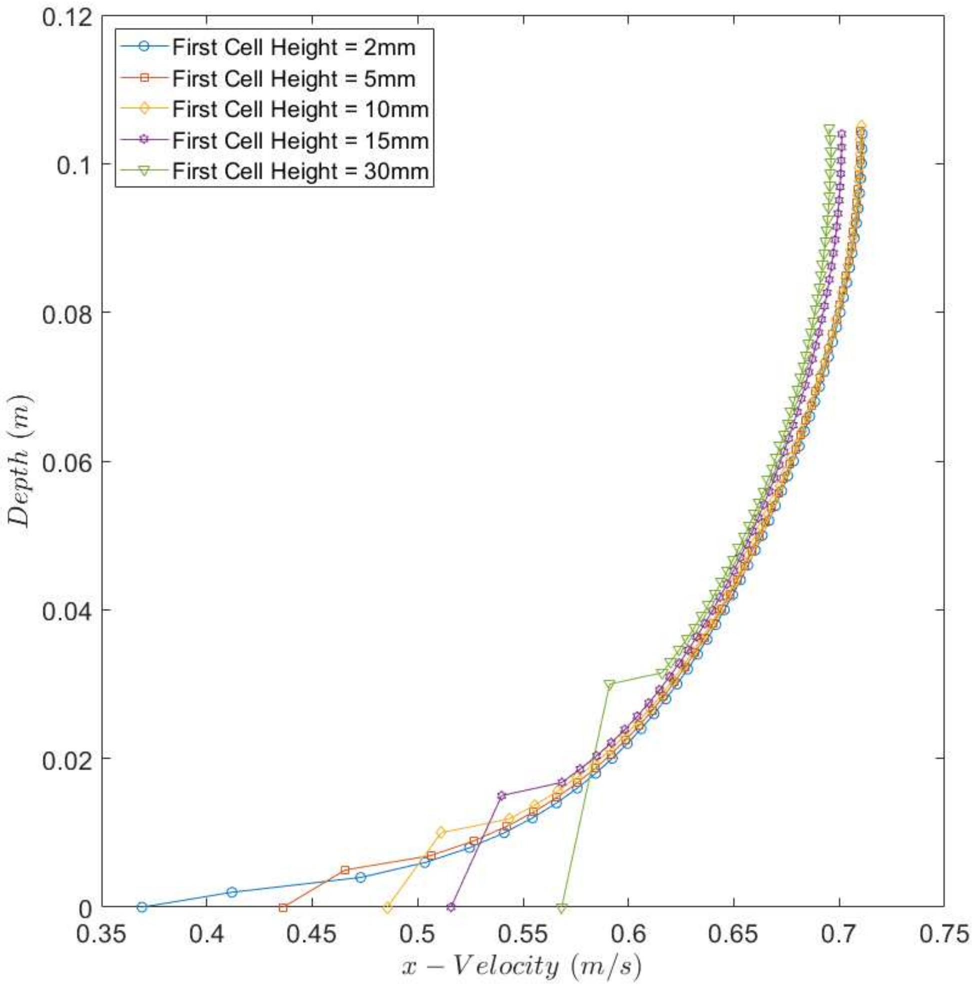

Figure 3.3 – Flow Velocity Profile Development Dependence on First-Cell Height.

3.2 - Downstream Distance Sensitivity

The second initial study conducted was to determine the effect that the specified distance downstream of the weir might have on the model. Three separate models were created with varied downstream distances: 2 m, 3.5 m, and 7 m. A 2D model flume with a 0.3 m high sharp-crested weir at 15 m from the inlet was constructed. The grid cell resolution in the horizontal direction was 1 cm while the vertical resolution was 5 mm. A volumetric inflow and uncontrolled outlet were used as the boundary conditions. Only the distance downstream of the weir was altered between models.

The velocity profile 1.5 m upstream from the weir and the crest velocity and pressure profiles were then analyzed for differences between the simulations. Figures 3.4 and 3.5 display the respective results. Between each downstream distance simulation, there were no changes in the simulated upstream results. This result was expected given that in a free-flow condition is not affected by downstream flow conditions. Therefore, it was concluded that the simulated weir results to be considered in this study are independent of the downstream mesh for free-flow conditions.

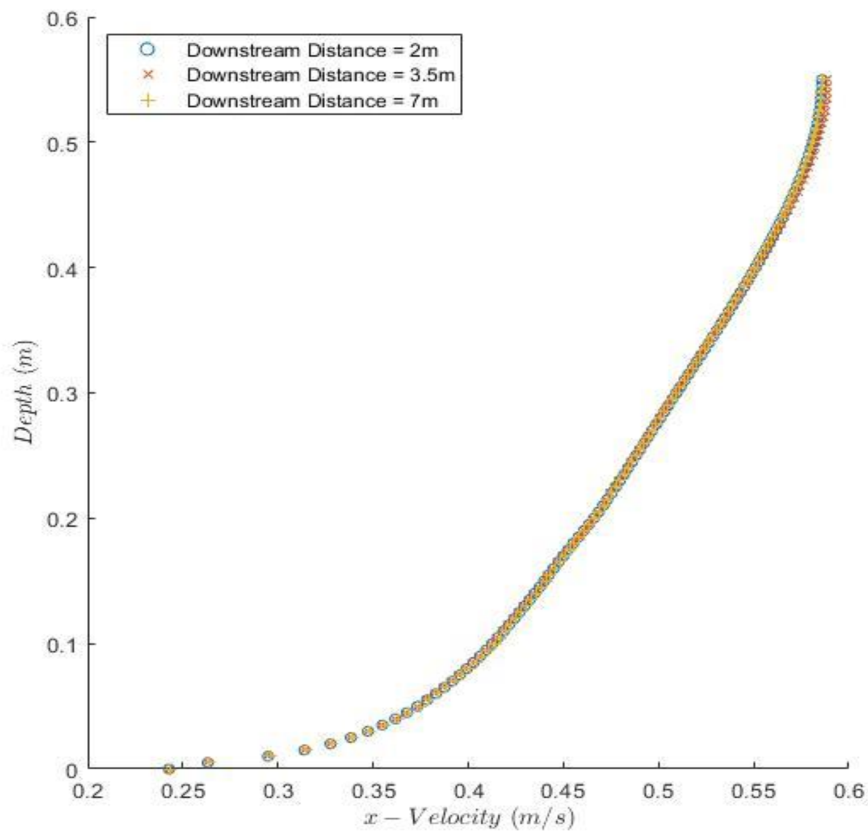

Figure 3.4 - Upstream Developed Velocity Profiles for the Downstream Distance Study.

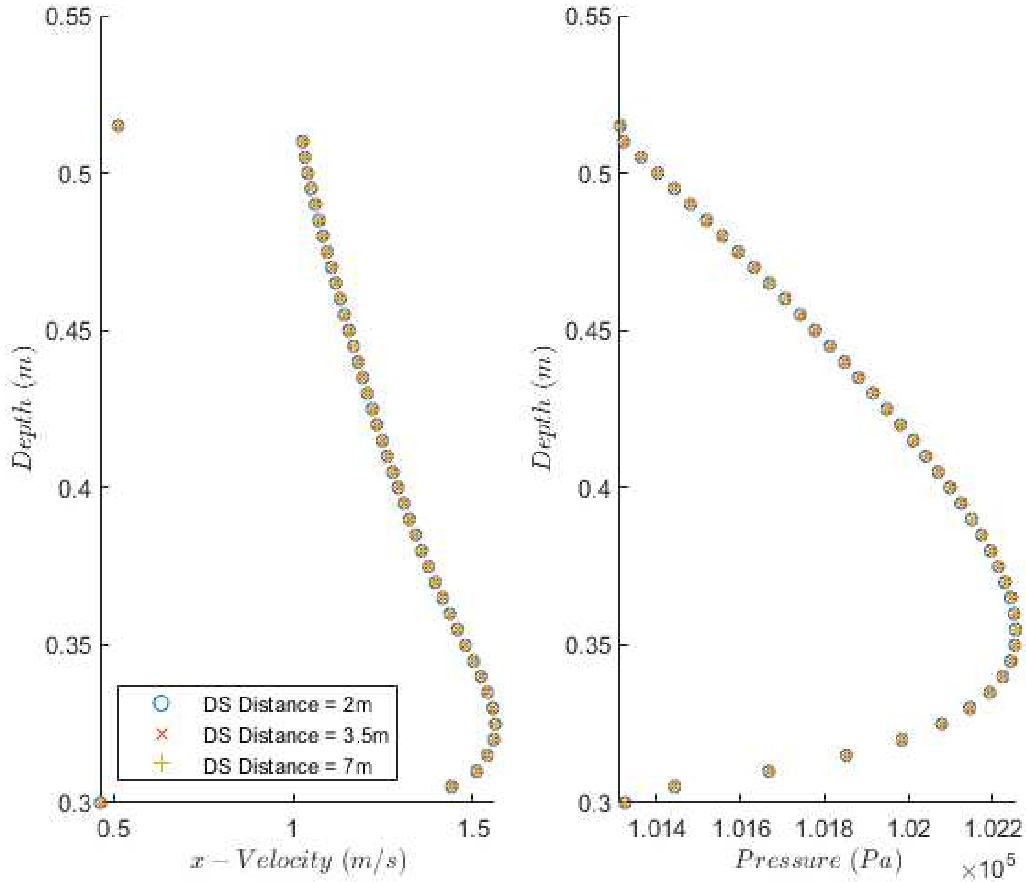

Figure 3.5 - Crest Velocity and Pressure Profiles for Downstream Distance Study.

3.3 – Conclusions on Use of FLOW-3D

To build more accurate and reliable simulations with FLOW-3D, several studies were conducted. Analysis of simulated flow development led to the conclusion that additional channel length should be specified to allow the simulated flow to fully develop. The length of the upstream region would depend on the scale and geometry of the flow region, so velocity profiles would be checked for development in each simulation. The size of the first cell adjacent to the simulated flume bottom also had to be analyzed to insure compliance with the regulations of FLOW-3D's code. The log-law is used to calculate the velocity in this first cell and the y^+ value is recommended to be within a certain range. A first-cell height of roughly 2 mm was found to be suitable for the scale of models used in the following studies. Finally, the prescribed distance downstream of a free-flowing sharp-crested weir was analyzed for impacts on the simulated upstream flow. Results indicated that the prescribed channel length downstream will have no effect on the simulation as long as the channel outlet extends beyond the free-flowing nappe region.

CHAPTER 4 – SHARP-CRESTED WEIR STUDY[1]

4.1 – Objective of the Sharp-Crested Weir Study

While numerous studies have been conducted on the sharp-crested weir, there has been little done on exploring the ideal conditions for operating a sharp-crested weir as a flow measurement structure. Furthermore, exploring flow patterns and properties surrounding the weir under a variety of conditions has yet to be done. A parametric study was conducted to utilize CFD's versatility and imaging to delve into these topics at the lab scale for a sharp-crested weir. Velocity and pressure profiles over the crest of the weir for a variety of flow rates were analyzed as well as the eddy length (L_e) and height (h_e) upstream of the weir. Multiple discharge coefficients were also calculated using both Equations 1 and 2, as well as Equation 4.

4.2 - CFD Models of the Sharp-Crested Weir

The flume and weir geometries for the CFD model were based on laboratory work of by Rajaratnam (1971). In this study, two models, A and B, were used. The modeled flume for the A experiments was 0.3 m wide with a weir also 0.3 m high and 0.005 m in thickness. The length of the flume in the CFD study was 20 m long to allow for flow to develop fully prior to reaching the acceleration zone of the weir. Fully-developed flow in the approach is an important assumption in the weir rating equations. The weir was placed at a distance of 15 m downstream from the inlet of the flume, leaving a 5 m downstream distance for simulated flow to exit the simulation. In the B experiments, the flume was 0.45 m wide and 10 m long. The modeled weir was 0.03 m high and 0.0015 m thick and placed 8 m from the upstream inlet. Sufficient upstream length was

[1] A manuscript based on the work of this chapter has been submitted to the Journal of Irrigation and Drainage. The title of the work is "Some Insights on Flow Over Sharp-Crested Weirs using Computational Fluid Dynamics: Implications for Enhanced Flow Measurement" by J. M. Sinclair, S. K. Venayagamoorthy and T. K. Gates.

also provided in these experiments to allow flow to develop. The vertical height or depth of the flume was varied depending on the expected depth of simulated flow in the model.

Mesh resolution for the A models was 1 cm in the horizontal x-direction and 5 mm in the vertical y-direction. This was reduced to 5 mm in the x-direction and 2.5 mm in the y-direction for the B models. In both sets of models, y^+ values were checked to ensure they were within the log region of the flow. A single cell was used in the lateral z-direction, making both models 2-dimensional. Due to the large number of simulations that had to be run in this parametric study, it was more efficient to run 2D models and thereby reduce the number of required cells in the models. Furthermore, in an open-channel section with no bends or other hydraulic structures, flow tends to have very little lateral flow. Therefore, the only changes in flow quantities occur in the vertical and horizontal directions. An image of a section of the mesh for the A simulation is presented in Figure 4.1.

To better resolve the weir geometry, a nested mesh with finer resolution was used. It spanned the height, width, and thickness of the weir and had a finer resolution than the outer mesh. In the A models, the nested mesh had an x-direction resolution of 2.5 mm and a y-direction resolution of 5 mm. The B models x-direction resolution as 2.5 mm and 1.25 mm in the y-direction. The lateral resolution was made 3D by adding 30 to 45 cells to eliminate the possibility of holes in the weir. Since the fluid would not come into contact or be simulated on this mesh, it was deemed appropriate to use a 3D mesh.

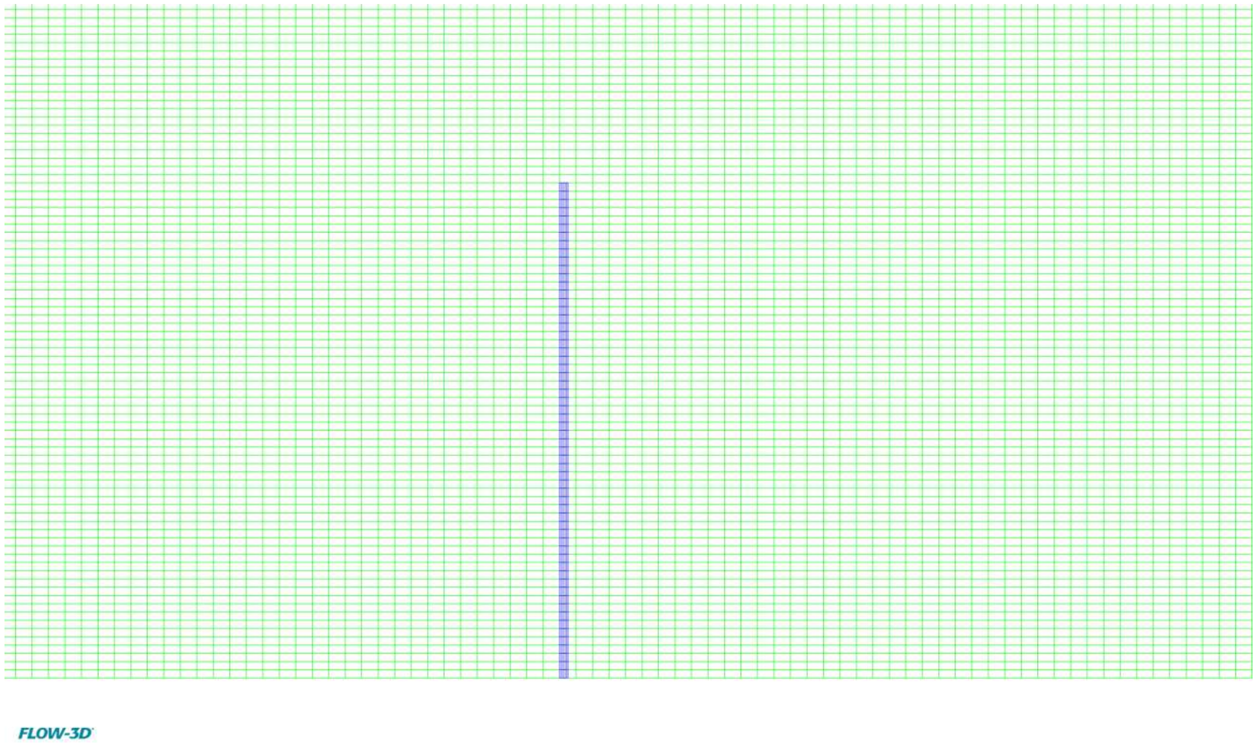

Figure 4.1 - Mesh Section for the A Models in the Sharp-Crested Weir Study.

An RNG k-ε turbulence model was used for all simulations in this study. The pressure was solved implicitly using a GMRES scheme while the momentum advection and viscous stress solvers were both first-order explicit schemes.

Boundary conditions were set in a manner to make each model an accurate representation of a lab flume as possible. The inlet condition at the upstream of the model domain was specified a volumetric flow rate. The inlet flow was aligned in the positive x-direction without vertical or lateral components. In the A and B models, fluid entered the mesh over the entire upstream inlet. In the validation studies that will be presented later, the inflow was given a specified depth to make the models as similar to the experimental studies as possible. The downstream boundary condition for the A models was an outlet, where simulated fluid was allowed to exit without having to reach a certain condition, such as a specified height or pressure. For the B models, a pressure condition was used to specify a fluid depth the simulation had to reach before exiting the mesh to help the flow achieve a subcritical state. A downstream depth had to be specified given the large *h/P* values in the flow and the reduced influence of the weir. The bottom of the model flume was set as a wall boundary condition with zero roughness height. The no-slip condition is imposed here, but the zero roughness height would reduce the complexity of the flow. Laboratory flumes are designed to achieve as smooth a wall as possible, so this model boundary condition is ideal for simulating lab experiments. The upper vertical condition was a pressure outlet condition. If fluid were to reach the upper vertical boundary of the model, it would exit the simulation. However, the models were set up so this boundary would not be reached, making the upper boundary a failsafe. The side walls of the flume were specified to be symmetry conditions with zero normal fluxes, acting as walls without the no-slip condition of boundary layers.

The simulations were run with water at 20°C as the fluid using property values imported from FLOW-3D's databank. An initial fluid region was placed upstream of the weir to cut down on computational time. The pressure in this initial region was initially set to be hydrostatic. Once the simulation started, the fluid region upstream of the weir would change with the simulation. The simulated pressure would not remain hydrostatic, but rather would vary using the numerical methods explained earlier.

CFD models were set to run for 1,500 seconds in modeled time, based on estimates of the maximum time it would take simulated fluid to flow through the simulation several times in order to reach a steady-state. However, the model was set up to terminate once it had reached steady-state which was always prior to the 1,500 second mark. The criteria for termination was less than a 1% change in the total mass, average mean kinetic energy, average mean turbulent energy, and average mean turbulent dissipation between consecutive time steps.

4.3 – CFD Model Validation and Verification

Prior to running any model parametric study, the models had to be validated and verified using existing, well-accepted experimental data. Laboratory studies by Rajaratnam and Muralidhar (1971) provided adequate detail to both build and validate these CFD models. The models were validated by comparing the simulated non-dimensional velocity and pressure profiles over the crest of the weir to the laboratory observations for several experiments. The simulated upstream eddy length was also compared to those gathered from Rajaratnam and Muralidhar (1971). In their experiments, Rajaratnam and Muralidhar injected a dye close to the flume bed and measured to a point where the dye appeared gained an upward velocity component. Table 4.1 contains the laboratory experimental data used to validate the models. Non-dimensional velocity and pressure plots from Rajaratnam and Muralidhar (1971) were digitized using software.

Table 4.1 - Rajaratnam and Muralidhar (1971) Validation Experiment Trials.

Experiment Name	***P*** (m)	***H*** (m)	***h/P***	***Q*** (m^3/s)	L_e (mm)
RM A1	0.3	0.185	0.625	0.0525	4.45
RM A2	0.3	0.207	0.697	0.0623	4.78
RM B1	0.175	0.198	1.122	0.0606	5.41
RM C3	0.03	0.099	3.440	0.0420	-

The final results from the validation study are presented in Figures 13 and 14, where the RM initials indicate laboratory data from Rajaratnam and Muralidhar (1971). Figure 4.2 shows the velocity profiles at both the weir crest and Section 0-0 while Figure 4.3 depicts the pressure profiles at both locations. Vertical values above the crest are made non-dimensional by dividing by the total depth above the crest, y. Similarly, at Section 0-0, the vertical values are divided by the thickness of the nappe at that section, $\bar{y}$. Velocity was made non-dimensional by dividing by a reference velocity, $U = \sqrt{2gh}$. Pressure was divided by hydrostatic pressure, p_h, at the section, either γy or $\gamma \bar{y}$ for the weir crest and Section 0-0, respectively. Weir crest data is presented for all experiments, while only experiments A1 and A2 are shown in the Section 0-0 results as they were the only experiments to develop a nappe.

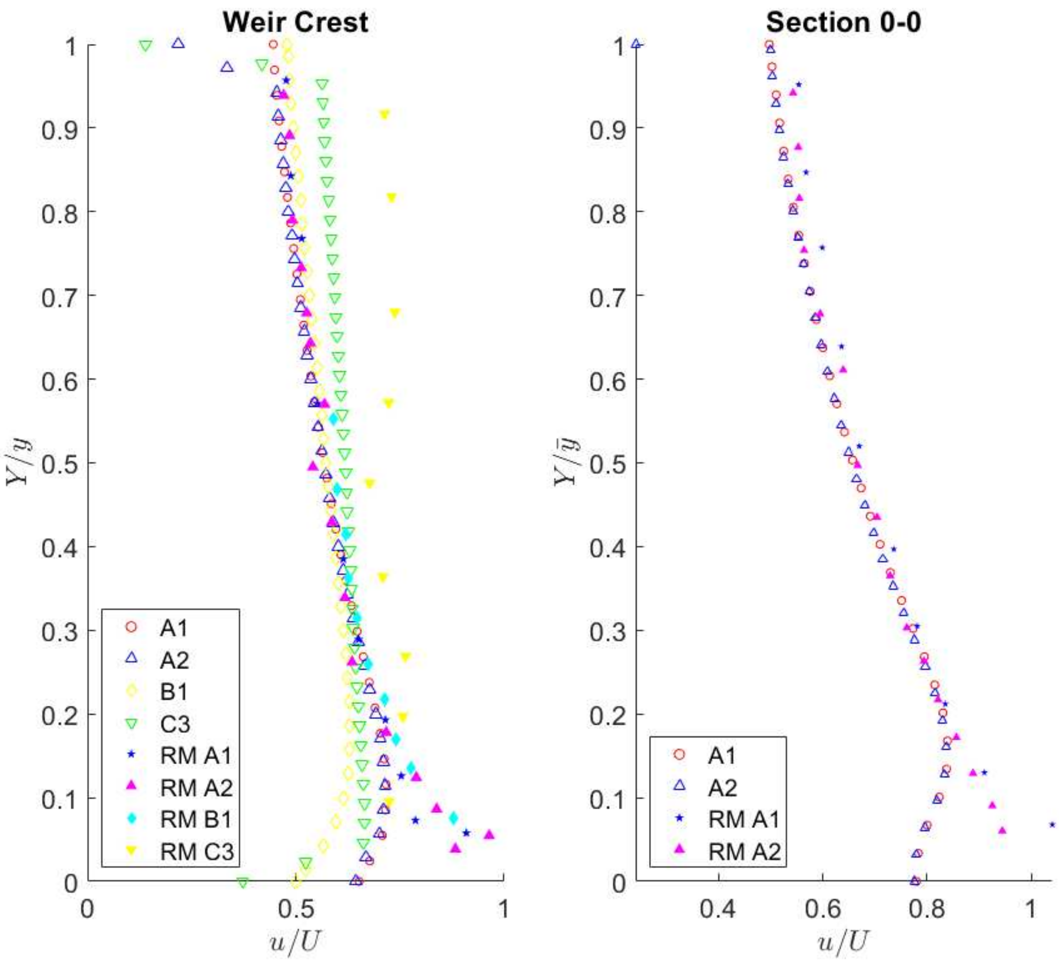

Figure 4.2 – Sharp-Crested Weir Simulated Velocity Profile Validation.

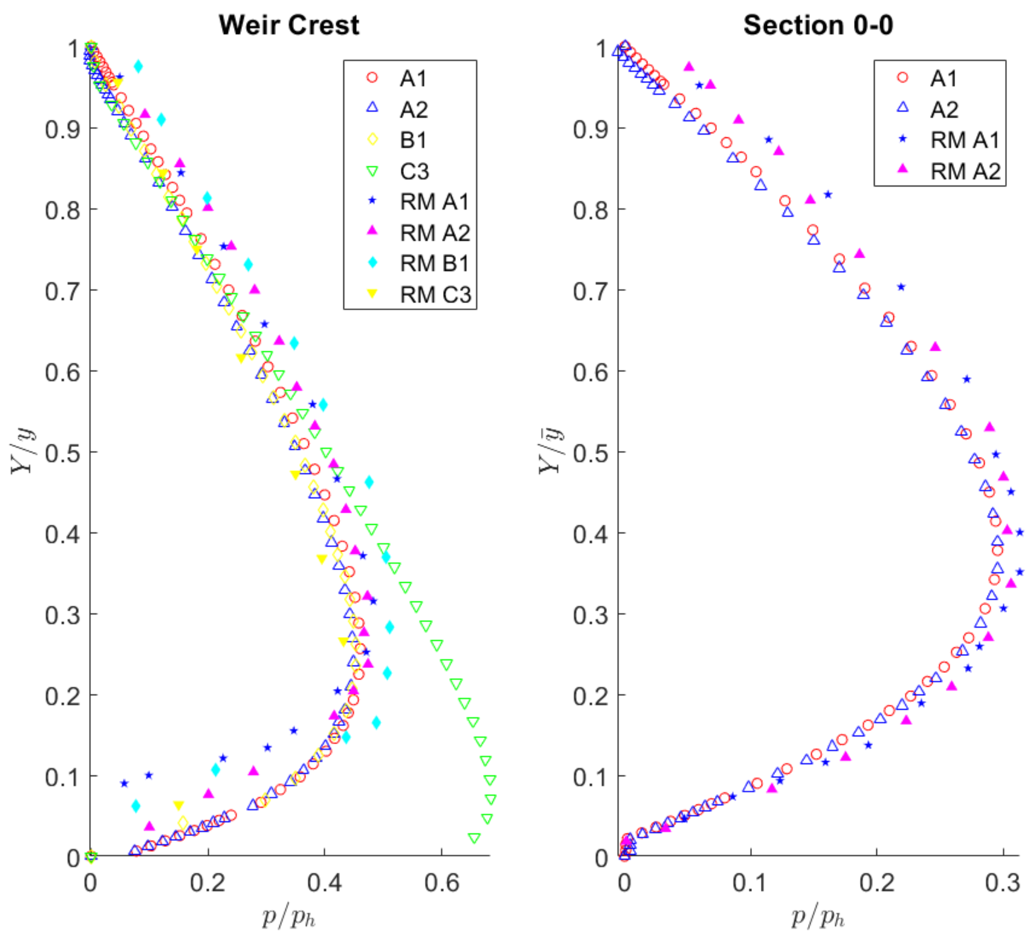

Figure 4.3 – Sharp Crested Weir Simulated Pressure Profile Validation.

The velocity validation showed good agreement to experimental results at the higher *y*-values, with each of the graphs collapsing on one another. At the lower *y*-values, the experimental results indicate a continued increase in velocity magnitude closer to the crest while the CFD results show a decrease in velocity magnitude in the approach to the weir crest, reaching a maximum value around a non-dimensional *y*-value of 0.1. In reality, the velocity exactly at the weir crest should be zero as a result of the no-slip condition. The decrease in relative velocity towards the weir crest indicates the CFD results may be more accurate. In either case, the agreement between the experimental and CFD studies at both the weir crest and Section 0-0 is reasonable.

Pressure results show a curved distribution with the pressure starting at roughly zero gauge pressure before increasing to a maximum relative value at a non-dimensional y-value between 0.2 and 0.3. The distribution depicts a decrease back to zero gauge pressure at the free surface. Results at Section 0-0 showed a similar trend, except with the maximum relative pressure at a non-dimensional *y*-value of about 0.4. Again, the differences between the CFD and experimental results were largest close to the weir crest. This can attributed to the difficulty of both experimentally measuring and calculating pressure with CFD in this active region. The difference between the model simulations and the lab trials decreases significantly at higher *y*-values.

In addition to the validation, several verification methods were used to check the physics of the model. A conservation of mass check upstream and downstream of the weir was performed with the velocity and area of flow. With the boundary conditions set as they were, the model could only have a certain amount of simulated fluid flow at a given time. If the calculated flow rate exceeded or was less than the imposed flow, this would indicate the presence of holes in the mesh or errors in the solver. However, after checking each model, it was found that conservation of mass was satisfied.

It was also important for the simulated flow to be fully-developed prior to reaching the acceleration zone upstream of the weir. Analyzing simulated velocity and pressure profiles at a number of distances upstream of the weir revealed that flow was indeed fully-developed. Figure 4.4 plots these profiles a three upstream locations for the h/p = 0.38 trial. Velocity and pressure profiles at all locations collapse, respectively, on one-another, indicating that the flow is fully-developed. The simulated velocity profiles are in the characteristic turbulent flow shape while the pressure distribution is hydrostatic in the developed, undisturbed region. Both of these results were expected and a similar analysis was done for each simulation.

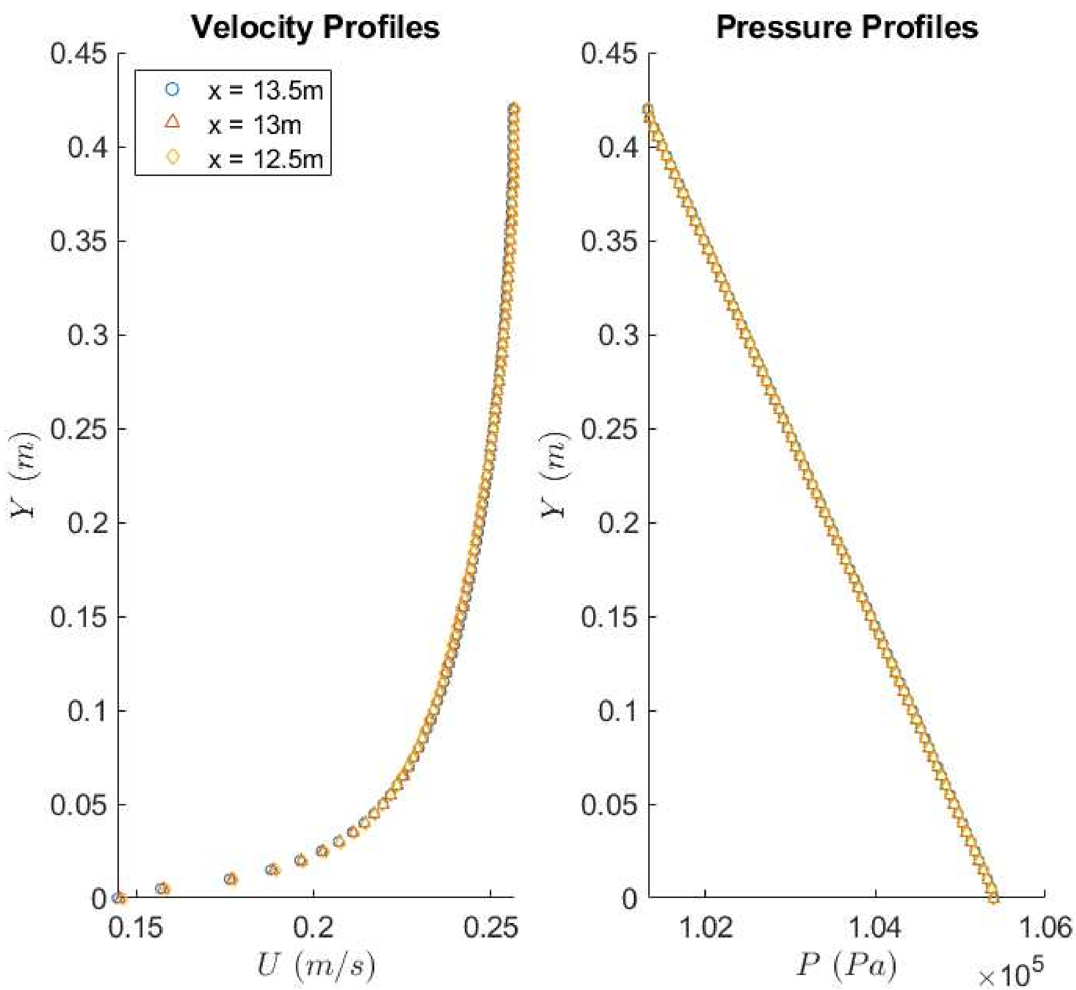

Figure 4.4 – Sharp-Crested Weir Velocity and Pressure Profile Development at Difference Locations Upstream of the Sharp-Crested Weir.

4.4 – Sharp-Crest Weir Parametric Study Results and Discussion

The calculated discharge coefficients C_d, C_{dR}, and C_{dT}, found using Equations 1, 2, and 4 respectively, are presented in Table 4.2 along with the L_e/P and h_e/P values.

Table 4.2 – Sharp-Crested Weir Parametric Study Variables.

Trial Name	*H/P*	*h/P*	*Q* (m^3/s)	*P* (m)	C_d	C_{dT}	C_{dR}	L_e/P	h_e/P
A1	0.388	0.378	0.03	0.3	0.887	0.854	0.633	0.55	0.27
A2	0.441	0.429	0.035	0.3	0.857	0.821	0.638	0.53	0.27
A3	0.492	0.477	0.04	0.3	0.834	0.796	0.642	0.53	0.24
A4	0.600	0.579	0.05	0.3	0.779	0.738	0.650	0.58	0.28
A5	0.647	0.625	0.0525	0.3	0.730	0.694	0.654	0.60	0.28
A6	0.684	0.660	0.0623	0.3	0.798	0.757	0.657	0.60	0.29
A7	0.705	0.679	0.06	0.3	0.738	0.697	0.658	0.62	0.30
A8	0.780	0.747	0.07	0.3	0.744	0.698	0.664	0.63	0.30
A9	0.853	0.813	0.08	0.3	0.750	0.698	0.669	0.63	0.30
A10	0.925	0.878	0.09	0.3	0.752	0.695	0.675	0.58	0.24
A11	0.985	0.930	0.1	0.3	0.766	0.702	0.679	0.50	0.21
A12	1.059	0.997	0.11	0.3	0.759	0.693	0.685	0.50	0.21
A13	1.132	1.063	0.12	0.3	0.753	0.684	0.690	0.53	0.23
A14	1.382	1.280	0.16	0.3	0.759	0.677	0.708	0.67	0.30
A15	1.745	1.596	0.22	0.3	0.750	0.656	0.734	0.73	0.33
A16	2.160	1.944	0.3	0.3	0.761	0.649	0.763	0.83	0.37
A17	2.365	2.129	0.334	0.3	0.739	0.631	0.779	0.83	0.38
A18	2.681	2.375	0.41	0.3	0.770	0.641	0.799	0.83	0.38
B1	3.125	2.624	0.027	0.03	0.920	0.708	0.808	-	-
B2	3.770	3.129	0.035	0.03	0.916	0.693	0.846	-	-
B3	4.325	3.56	0.042	0.03	0.905	0.676	0.878	-	-
B4	4.939	4.041	0.05	0.03	0.892	0.660	0.914	-	-
B5	5.615	4.545	0.06	0.03	0.897	0.653	0.952	-	-

Three distinct flow regimes were identified after analyzing the velocity and pressure profiles.

The velocity and pressure profiles over the weir crest and presented in Figures 4.5 and 4.6, respectively, with a straight line on Figure 4.6 representing the hydrostatic pressure distribution. In first regime, where $h/P < 0.6$, a strong acceleration occurs near the weir crest; thus it is called the high-acceleration regime. Corresponding to this acceleration was a drop in simulated pressure that with relative gauge pressure becoming negative. Velocity profiles display a decrease in relative velocity magnitude as h/P increases. The largest decrease comes in the region close to the weir crest. Pressure profiles also depict increase in pressure relative to atmospheric pressure as the velocity decreases. Often in this region, flow can be seen clinging to the weir for $h/P < 0.5$, indicating surface tension and viscous effects influencing the flow.

The second regime was named the ideal-operating regime and occurs for $0.6 < h/P < 2.0$. The respective velocity and pressure profiles collapse on one another in this regime. The acceleration region close to the weir crest becomes smaller, indicating no negative pressure in that vicinity. Pressure profiles indicate pressure beginning at atmospheric and increasing to a maximum value at a non-dimensional *y*-value of 0.15. The pressure profile then decreases linearly as the *y*-values increase. The nappe tends to be well formed and the flow is well-behaved in relation to the assumptions, underscoring on the ideal-operating regime.

The simulated weir flow tends to become inundated for $h/P > 2$ with both the pressure and velocity profiles beginning to diverge. This is dubbed the weir-inundated regime. The velocity profiles look more like that for a turbulent boundary layer flow as the weir effects become drowned out. Similarly, the pressure profiles approach that for a hydrostatic pressure distribution. In flow with $h/P > 3$, the weir becomes submerged, with downstream flow conditions affecting the simulated flow upstream of the weir.

After identifying and analyzing each of these regimes, the ideal operating range for the sharp-crested weir is determined as $0.6 < h/P < 2.0$. Not only is the flow fully-developed prior to reaching the weir, but the nappe is often well-formed with atmospheric pressure beneath. The regime for these h*/P* values is also not subject to the excessive acceleration or inundation that occurs at lower or higher *h/P* values, respectively. The flow-acceleration and inundation introduce too many irregularities which influence the flow surrounding the weir.

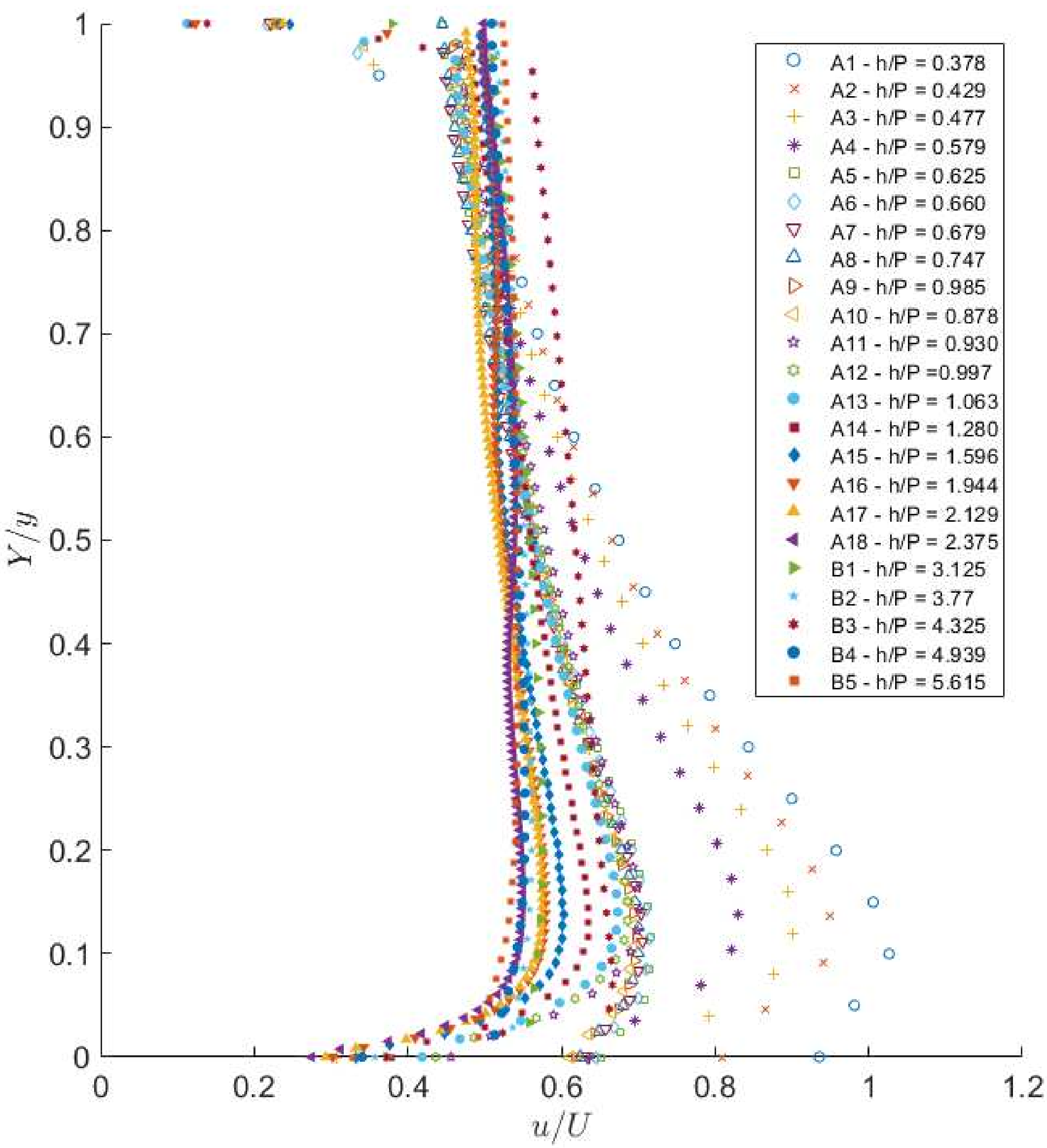

Figure 4.5 - Non-dimensional Velocity Profiles over Sharp-Crested Weir Crest.

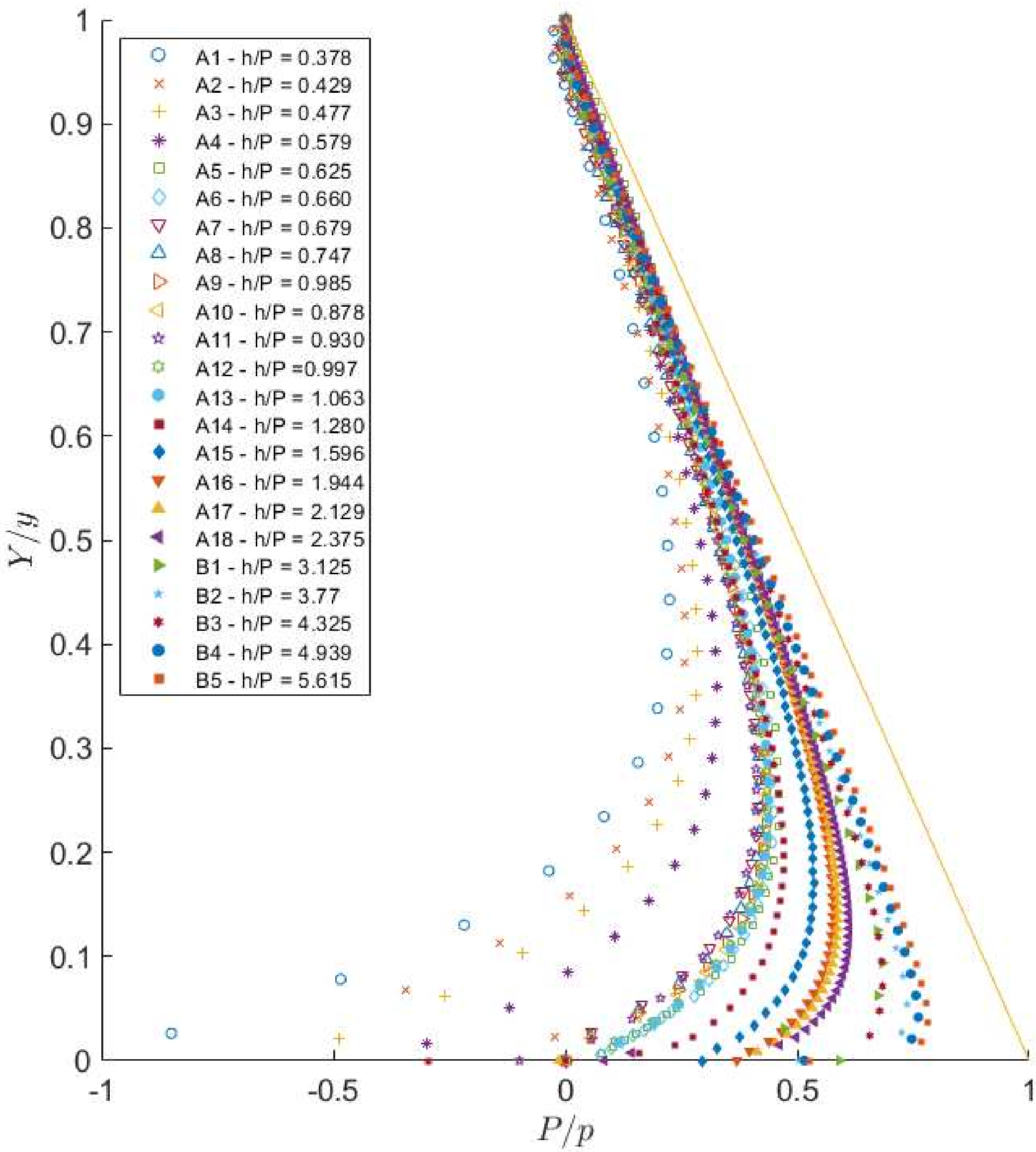

Figure 4.6 - Non-dimensional Pressure Profiles over Sharp-Crested Weir Crest.

Plotting the calculated discharge coefficients also reveals these three regimes, as show in Figure 4.7. The dashed vertical lines in the plot represent the relative transition points for each operating regime. The high-acceleration regime is in the section on the far left, the ideal-operating regime is between each dashed line, and the weir-inundated regime is to the right of the second dashed line. For $h/P < 0.6$, both C_d and C_{dT} decrease linearly in the flow-accelerating regime. In the ideal-operating regime where $0.6 < h/P < 2$, the coefficient becomes relatively constant, with the coefficient of variance being about 0.022 for C_d and C_{dT}. The value of C_d hovers around 0.75 while C_{dT} is below 0.7. The discharge coefficient trends for $h/P < 1.2$ are consistent with experimental data obtained by Johnson (2000). For $h/P > 3$, C_d and C_{dT} values jump up, likely due to the inundated or submerged conditions of the flow. For consistency, the discharge coefficients in the weir-inundated regime were calculated in the same manner as for the other regimes. There was no adjustment for submergence through the introduction of empirical constants, as is often done in practice.

The Rehbock discharge coefficient, C_{dR}, increases linearly as h/P increases, a trend that is markedly different than the calculated C_d and C_{dT} trends. Although Henderson (1966) stated the Rehbock equation had good agreement with experimental results up to $h/P < 5$, it is clear that using said equation incorrectly represents the trend of C_d. The Rehbock equation should be altered to account for the actual trend seen in C_d. Caution should also be exercised in using the Rehbock equation for an estimate of discharge coefficient if accurate results are desired.

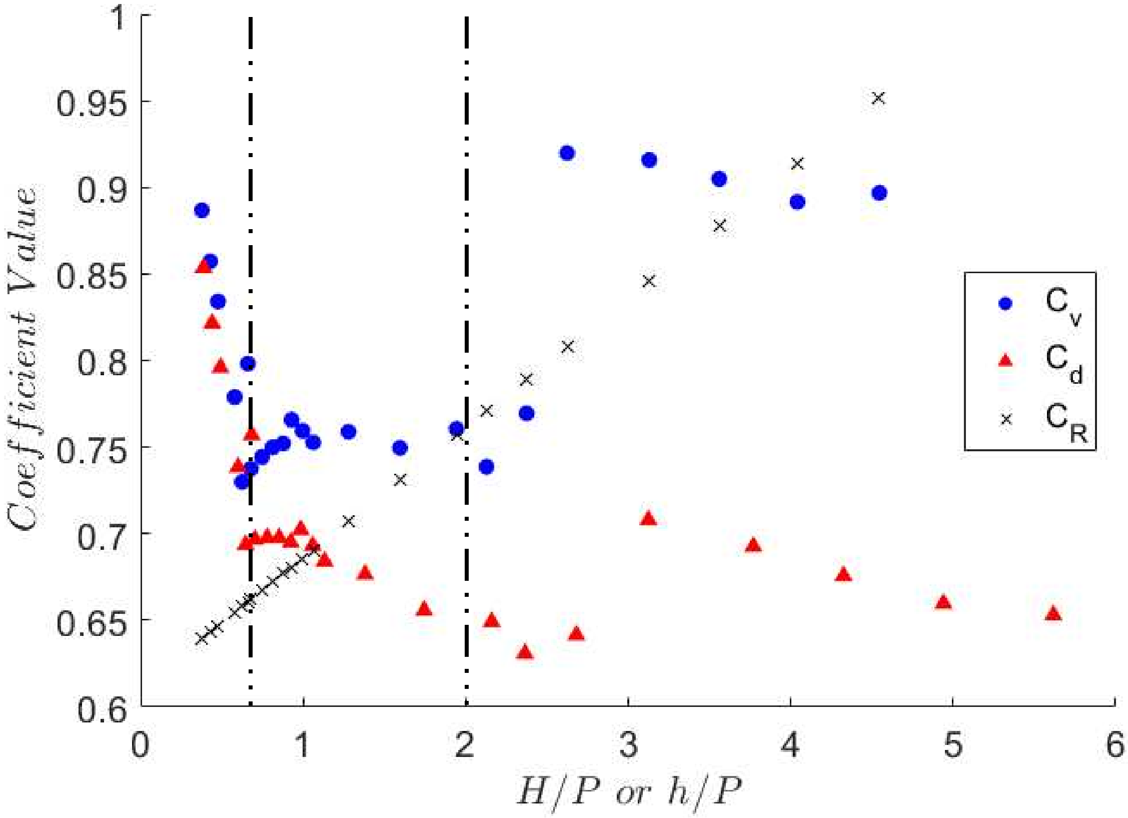

Figure 4.7 - Discharge coefficients as function of *h/P* (for C_d and C_{dR}) and of *H/P* for C_{dT}.

Given the near constant value of C_d in the ideal-operating range, a test was conducted to estimate how much error would be introduced when using a constant value of C_d for a number of different flow rate calculations. A C_d of 0.75 was selected as the constant value and flow rate, Q, was calculated using the rating equation and known variables of the flow. The calculated Q was compared to the simulated actual Q, depicted in Figure 4.8. Results show an excellent agreement indicating that, for the ideal-operating range, a constant C_d can be used to calculate Q with adequate accuracy.

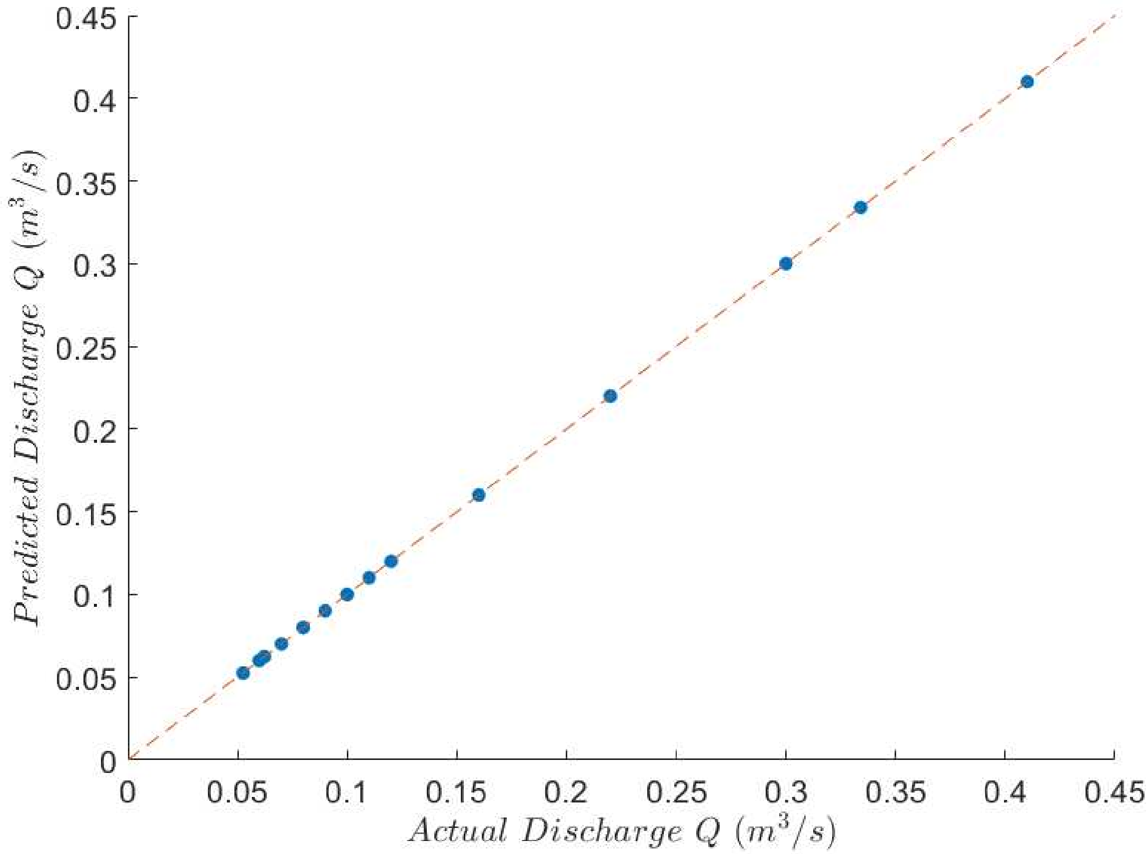

Figure 4.8 - Comparison of predicted discharge using $C_d = 0.75$ versus actual discharge. The dashed line shows the one to one correlation.

Velocity contour plots were also created to visually analyze how the flow changes with *h/P*. Figures 4.9 through 4.11 are velocity magnitude contours for three different simulations: *h/P* = 0.38, 0.81, and 4.55. These *h/P* values were chosen because each was characteristic of the three regimes discussed earlier. In Figure 4.9 for *h/P* = 0.38 in the high-acceleration regime, flow clings to the weir and velocity increases at the weir crest, resulting in negative gauge pressure. For *h/P* = 0.81, in Figure 4.10, shows a well-formed nappe with no excessive acceleration or negative pressure at the weir crest, as expected in the ideal operating regime. Finally, in Figure 4.11 with *h/P* = 4.55, the weir is inundated and submerged, not acting as an effective control or measuring structure. As *h/P* increases beyond this, the weir will act more as a sill with its effects on the flow lessened greatly.

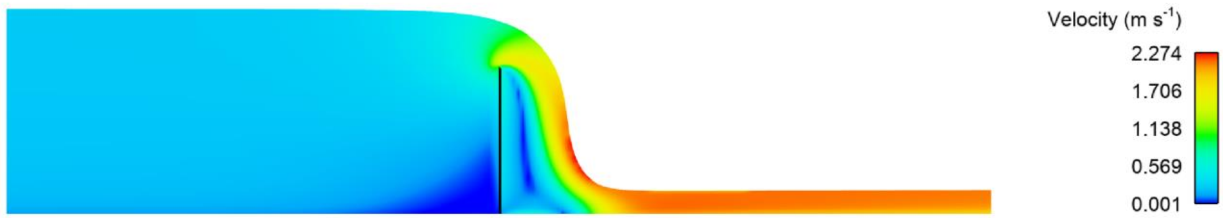

Figure 4.9 - Velocity magnitude contours for *h/P* = 0.38 depicting a clinging flow conditions due to the low relatively low head over the weir.

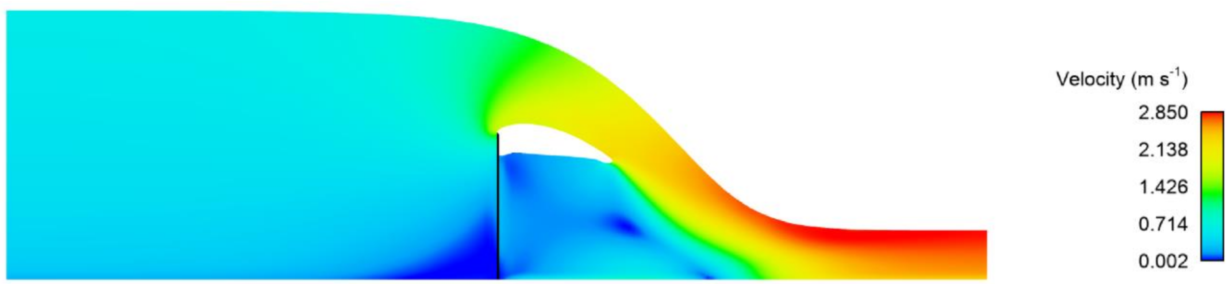

Figure 4.10 - Velocity magnitude contours for *h/P* = 0.81 depicting an ideal operating flow condition over the weir.

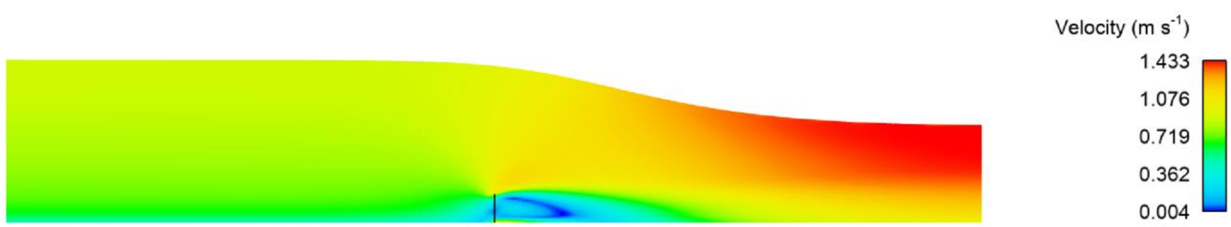

Figure 4.11 - Velocity magnitude contours for *h/P* = 4.55 depicting a weir-inundated flow condition over the weir.

The turbulent regions upstream of the weir can be seen in Figures 4.9 – 4.11 as the dark blue triangular shape directly upstream at the base of the weir. Flow recirculates and is caught within a larger eddy here as it cannot easily navigate over the weir without significantly changing velocity. The relatively lower velocities in this region are associated with a loss of momentum.

In addition, the visual depiction of the upstream turbulence patterns can be quantified. Eddy length, L_e, and height, h_e, were measured at points where the streamlines begin to separate from the main flow and create recirculating flow. For L_e, the measurement started at the point upstream of the weir where the velocity vectors gain significant vertical component and the recirculating vectors meet each other. The distance from said point to the weir was recorded. The value of h_e was similarly measured from the point where velocity vectors separated horizontally to continue either over the weir or down into the recirculation zone.

Figures 4.12 plots the non-dimensional eddy measurements against *Re*. Again, the dashed vertical lines in the plot represent the relative transition points for each operating regime. The high-acceleration regime is in the section on the far left, the ideal-operating regime is between each dashed line, and the weir-inundated regime is to the right of the second dashed line. It indicates similar nonlinear relationships of *Re* with both L_e and h_e. L_e and h_e initially decrease in magnitude with *Re* before increasing to a local maximum at about *Re* ~ 50,000. The values then decreases in size to a minimum at about *Re* ~ 70,000 before increasing once again to approach a maximum at about *Re* ~ 140,000. The trends seen here are markedly different than those in Rajaratnam and Muralidhar (1971), who state that L_e only increases with increasing *h/P* or *Re*. CFD's ability to more accurately capture and visualize flow eddies makes it likely more reliable than the dye method.

Eddy size in the high-acceleration regime initially begins at a low value before increasing until the ideal-operating regime range, which begins at about *Re* = 40,000. Both L_e and h_e begin to decrease in magnitude at the start of the ideal-operating regime. The minimum eddy size is within the ideal-operating range, again adding to the idea that flow is more efficiently controlled in this regime. The small eddy size means simulated flow can more easily navigate over the weir crest without becoming trapped in a recirculation zone. In the weir-inundated regime, where *h/P* > 2.00 or *Re* > 150,000, L_e and h_e are relatively constant in their respective values. These values approach a maximum value, meaning more simulated flow is trapped within a recirculation zone. The weir is no longer able to efficiently control flow, resulting in a large eddy size.

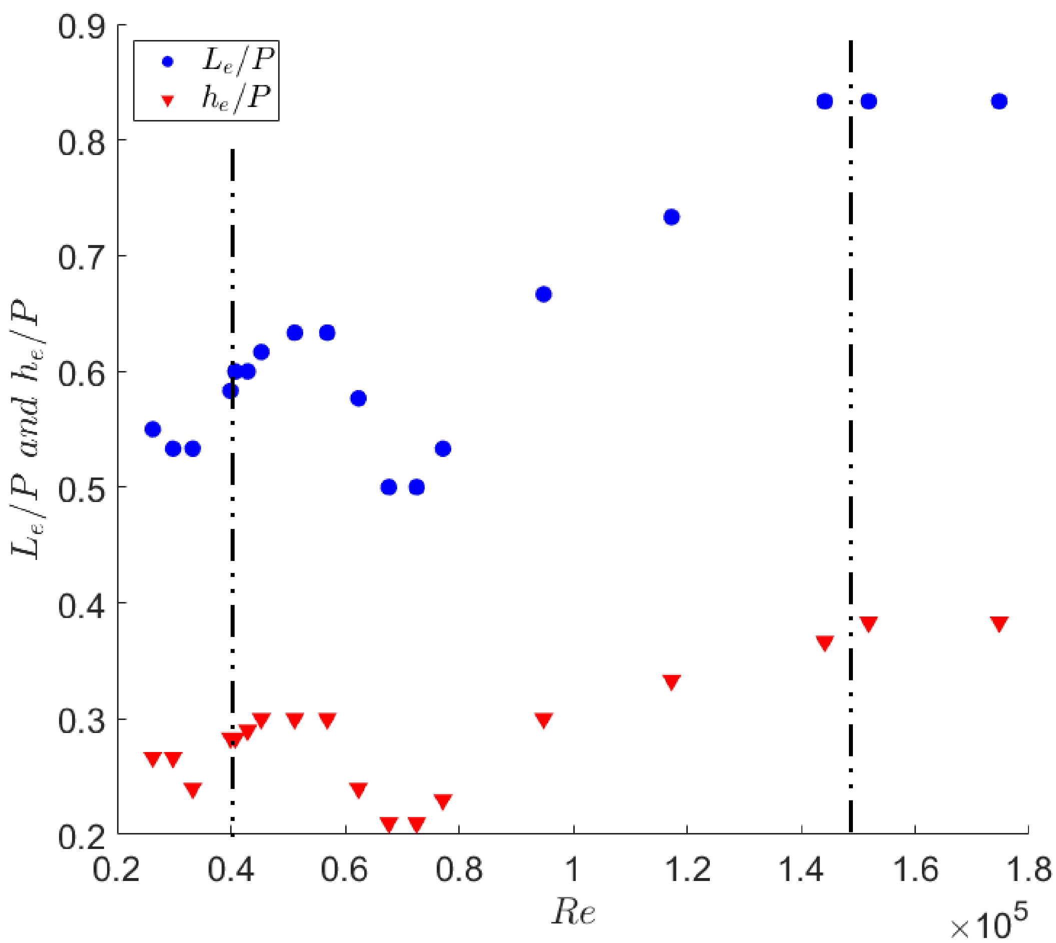

Figure 4.12 - Non-dimensional Eddy Dimensions, L_e and h_e, plotted against *Re*.

4.5 – Conclusions for the Sharp-Crested Weir Study

Three operating regimes were identified for flow over a sharp-crested weir using CFD to analyze the velocity and pressure distributions over the weir crest. The first, where *h/P* < 0.6, is the high-acceleration regime where flow accelerates close to the weir crest, resulting in a region of negative gauge pressure. The ideal-operating regime is defined for $0.6 < h/P < 2$. Here, the assumptions inherent in the rating equation appear to hold, with a well-formed nappe and lack of flow irregularities. For $h/P > 2$, the weir's effect becomes drowned out, hence constituting the weir-inundated regime. Downstream effects influence upstream flow as the weir is submerged with the velocity profile looking more like a turbulent boundary layer profile. Pressure begins to approach a hydrostatic profile as well.

Analysis revealed changes in C_d and C_{dT} for the three flow regimes. It was concluded that, in the ideal-operating regime, a constant C_d value could be used to estimate Q from the rating equation with reliable accuracy. Furthermore, it was found that the Rehbock equation was a poor predictor of C_d having little consistency with simulation results.

Finally, analysis of turbulence patterns upstream of the weir showed a correlation between the eddy size and *Re*. The minimum eddy size occurs at about $Re = 70{,}000$ and increases steadily to a constant values at about $Re = 140{,}000$. The trend seen in the CFD results does not match those previously found in Rajaratnam and Muralidhar (1971) where the eddy size was seen to only increase with *Re*.

CHAPTER 5 – PIVOT WEIR STUDY

5.1 – Objective of the Pivot Weir Study

The pivot weir is still a relatively new subject of study. The purpose of this investigation was to analyze behavior of flow over a pivot weir given the results obtained from the sharp-crested weir study to identify how the function of an inclined sharp-crested weir might change as either the inclination angle or flow rate changes. The velocity and pressure profiles over the weir crest as well as the discharge coefficient were considered. Furthermore, flow structure surrounding the weir was analyzed using visual velocity and pressure contours.

5.2 - CFD Models of Pivot Weirs

The models in this study are largely similar to those in the sharp-crested weir study; 2D, one-fluid models were used. The flume and pivot weir geometry were partially based on an experimental study set to be run in EFML at Colorado State University. The model flume has a width of 0.3 m and a length of 4.5 m while the pivot weir, placed 4 m downstream from the inlet, had a total length of roughly 0.07 m and a thickness of 2.5 mm. Due to the reduced scale of the models used in this study, the additional upstream distance necessary to develop the flow in the sharp-crested weir study was not needed in this case. Flow would have ample distance to develop in the 4 m upstream of the weir.

Five angles of inclination were tested based on the angles used by Wahlin and Replogle (1994) in their study, but were slightly adjusted to better match feasible angles for the experimental weir. Angles of 90°, 72°, 57°, 47°, and 27° were selected based on their approximation to relatively nice vertical to horizontal ratios of 3:1, 1.5:1, 1:1, 0.5:1, along with the 90° vertical case. Six flow rates were modeled at each angle to produce a variety of *h/P* values: 1.22 L/s, 2.275 L/s, 3.235 L/s, 5.895 L/s, 9.705 L/s, and 11.2 L/s, respectively.

The computational mesh resolution in the x-direction was 5 mm while y-resolution was 2 mm. Since the models were 2D, there was only a single cell in the lateral z-direction. Similar to the sharp-crested weir study, a nested mesh had to be used to better resolve the weir geometry. It split the x- and y-resolution in half to 2.5 mm and 1 mm respectively. In the lateral direction, 30 cells were used to get rid of holes in the geometry.

An upstream volumetric flow rate inlet without prescribed depth was used to insure that the weir would act as the only control within the channel. As such, an uncontrolled outlet was used as well as two symmetry conditions for the flume walls and a wall with zero roughness height as the flume bed. The top vertical condition was specified as a pressure condition to allow the model's free-surface tracker to be used.

Like the sharp-crested weir study, an RNG k-ε turbulence model was used for all simulations in this study. The pressure was solved implicitly using a GMRES scheme while the momentum advection and viscous stress solvers were both first-order explicit schemes. The solution was marched in time with a first-order explicit scheme.

The fluid was specified as water at 20°C. To speed up the time to steady-state, an initial fluid region was placed just upstream of the pivot weir with a flow depth equal to the weir height. The models were set to run for 1000 seconds or to end when they reached steady-state, which was defined in the same manner as in the sharp-crested weir study.

A summary of the results for the each of the inclination angles is given in Table 5.1. The name of each simulation contains the inclination angle, as well as an indicator for the flow rate. It is noted that three simulations could not yet be completed: the 11.2 L/s and 9.705 L/s flow rates could not be run for the 72° weir while the 1.22 L/s flow could not be run with the 57° weir angle. Errors in the refined mesh led to time-step errors and a lack of convergence in the momentum terms. The three simulations could not be finished within the available time frame of this study and were omitted from the study for the time being.

Table 5.1 - Pivot Weir Parametric Study Variables.

Name	Inclination Angle (°)	*h/P*	*H/P*	*Q* (L/s)	*P* (m)	C_d	C_{dT}	*Re*
90Q1	90	0.170	0.171	1.22	0.07	1.064	1.047	2,597
90Q2	90	0.262	0.268	2.275	0.07	1.032	1.002	4,709
90Q3	90	0.389	0.398	3.235	0.07	0.812	0.785	6,461
90Q4	90	0.594	0.616	5.895	0.07	0.784	0.742	11,120
90Q5	90	0.817	0.864	9.705	0.07	0.800	0.737	17,304
90Q6	90	0.905	0.961	11.2	0.07	0.793	0.725	19,506
72Q1	72	0.235	0.237	1.22	0.065	0.729	0.720	2,617
72Q2	72	0.366	0.372	2.275	0.065	0.699	0.684	4,704
72Q3	72	0.461	0.471	3.235	0.065	0.703	0.681	6,512
72Q4	72	0.682	0.707	5.895	0.065	0.712	0.675	11,212
57Q2	57	0.416	0.425	2.275	0.056	0.721	0.700	4,901
57Q3	57	0.526	0.540	3.235	0.056	0.723	0.695	6,774
57Q4	57	0.769	0.804	5.895	0.056	0.745	0.697	11,669
57Q5	57	1.060	1.130	9.705	0.056	0.757	0.688	18,050
57Q6	57	1.160	1.245	11.2	0.056	0.763	0.687	20,367
47Q1	47	0.295	0.300	1.22	0.047	0.842	0.824	2,751
47Q2	47	0.469	0.482	2.275	0.047	0.785	0.753	5,197
47Q3	47	0.589	0.611	3.235	0.047	0.793	0.750	7,090
47Q4	47	0.846	0.900	5.895	0.047	0.839	0.765	12,230
47Q5	47	1.211	1.314	9.705	0.047	0.807	0.714	18,839
47Q6	47	1.334	1.457	11.2	0.047	0.806	0.706	21,294
27Q1	27	0.435	0.447	1.22	0.032	0.839	0.805	3,053
27Q2	27	0.658	0.689	2.275	0.032	0.841	0.784	5,516
27Q3	27	0.830	0.882	3.235	0.032	0.844	0.770	7,602
27Q4	27	1.216	1.334	5.895	0.032	0.867	0.755	13,076
27Q5	27	1.714	1.929	9.705	0.032	0.853	0.714	20,140
27Q6	27	1.888	2.141	11.2	0.032	0.852	0.705	22,727

5.3 – Verification of the Pivot Weir Study

One of the goals of this study was to closely compare the CFD results with laboratory experimental results for the pivot weir. However, given time constraints, the experimental data could not be compiled in time for validation of the CFD results and a validation similar to that in the sharp-crested weir study was not possible. Focus was instead put on verifying the CFD results to limit sources of error and to ensure that they are physically reasonable.

The first test was verifying that velocity profiles had fully developed prior to reaching the pivot weir. Figure 5.1 shows both the velocity and pressure profiles plotted at three distances upstream of the weir for the 57° weir angle at 5.895 L/s. Over a 0.5 m span, the profiles change very little and collapse on one another, indicating fully-developed flow. Not only do the velocity profiles have the characteristic shape of a turbulent boundary layer, but the pressure profiles also are hydrostatic. Each complies with the expectations for flow behavior far upstream of the weir. A similar analysis was conducted for each inclination angle and flow rate.

Further checks were made for conservation of mass. Using the calculated velocity for each cell and the area of fluid in each cell, a total flow at any point in the simulation can be calculated. A limited amount of flow can exist in the simulation at a given time, so comparisons were made of the calculated flow rate to the prescribed flow rate. The difference in the two flows was found to be negligible, with no holes or induced flow within the model.

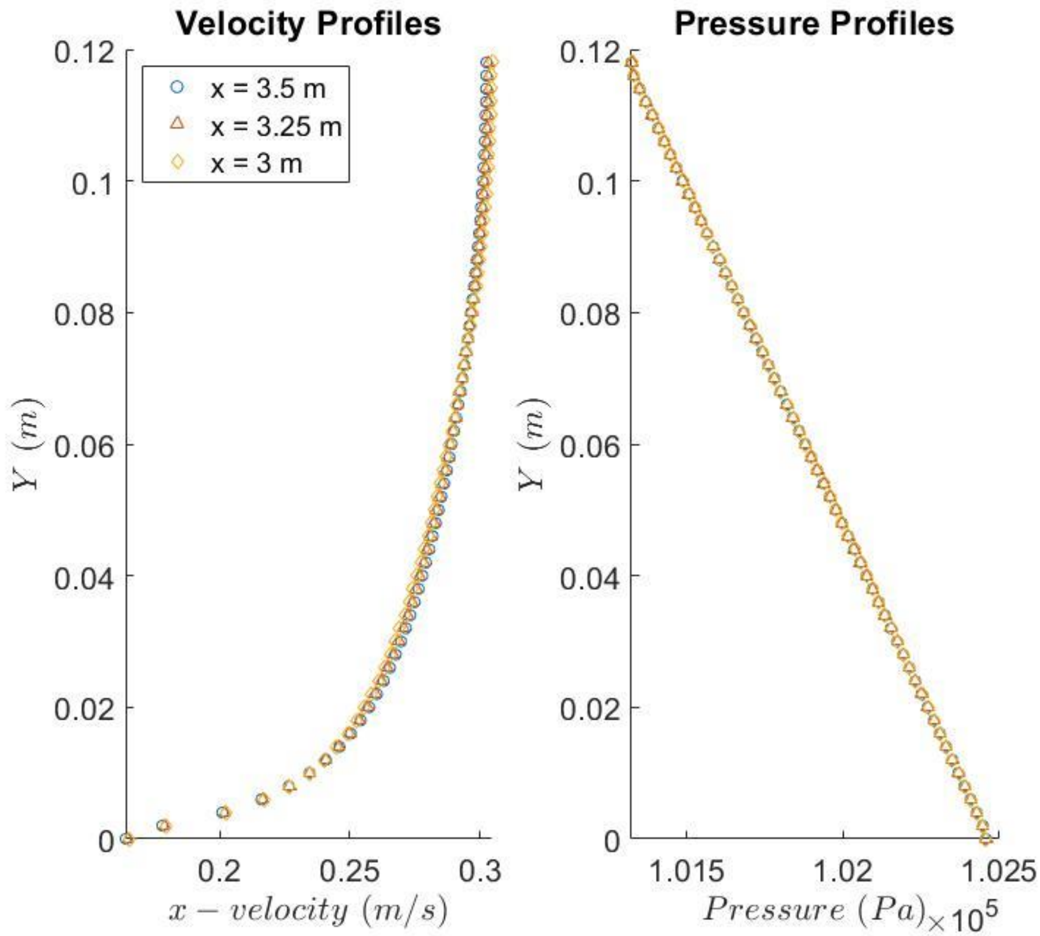

Figure 5.1 - Pivot Weir Velocity and Pressure Profile Development at Different Locations Upstream of 57° Weir for Q = 5.895 L/s.

5.4 - Pivot Weir Parametric Study Results and Discussions

Analysis of the simulation results provided insights into the behavior of the pivot weir, especially in regards how flow changes with a change in angle. Figure 5.2 plots *h/P* values for each value of Q and inclination angle. The *h/P* value at a constant flow increases as the angle of inclination decreases. If the findings from the sharp-crested weir study hold true, an increase in *h/P* at lower angles means a low inclination angle may be able to efficiently control a Q that would otherwise be outside the ideal-operating range of a higher inclination angle. A hypothesis is that the bounding flow rates for the ideal-operating regime would shift lower in value as the weir angle of inclination decreases. Where one flow may produce a lower *h/P* at 90° that is outside the ideal-operating regime, that same flow rate would produce a higher *h/P* at a lower inclination angle which could potentially lie within the ideal-operating regime.

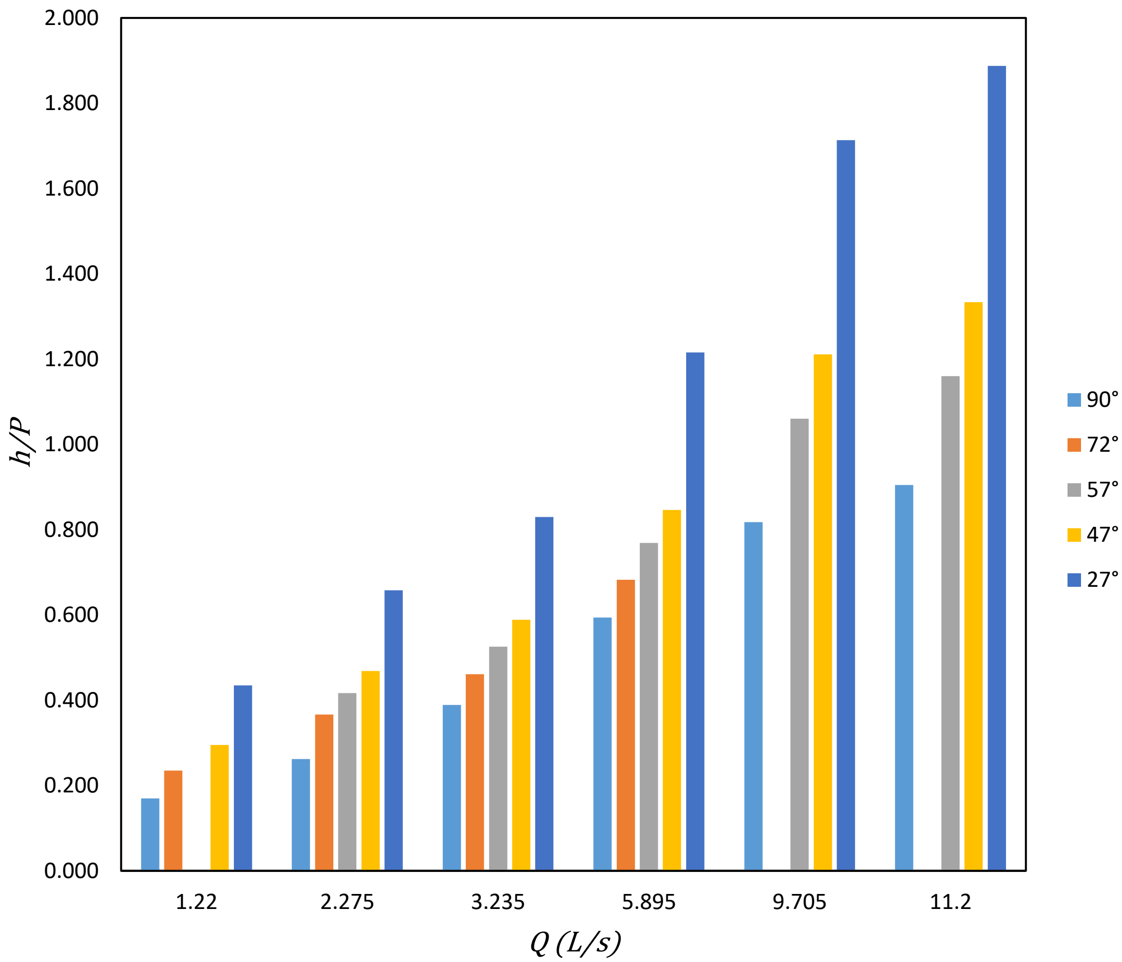

Figure 5.2 - Comparison of *h/P* for Varying Pivot Weir Angle of Inclination and Flow Rate.

The change in *H/P* is nearly identical to the *h/P* change, with *H/P* increasing for a constant *Q* as angle of inclination decreases. Figure 5.3 shows that as the inclination angle decreases, the there is an increase in the percentage of the total mechanical energy head that the velocity head makes up. An apparent outlier is the result for the 72° weir, but given the missing simulations at high flow rates, the 72° average velocity head would likely be higher and more in-line with the visible trend. An implication of the trend is that, at a lower weir angle, the relative velocity head increases at the expense of a decrease in flow depth. However, given the low weir height, the *h* remains high, as seen in the previous *h/P* results for each angle.

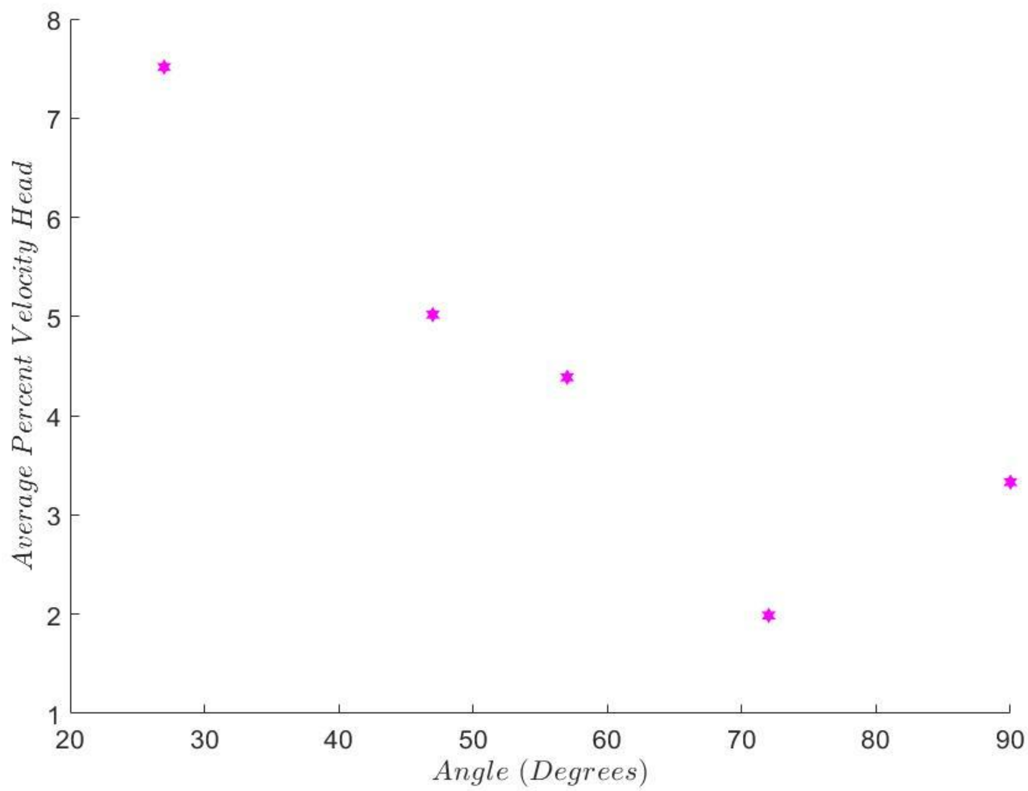

Figure 5.3 - Average Percent of H Composed of Velocity Head vs. Angle of Inclination of a Pivot Weir.

Discharge coefficient calculations also provide some useful insights in the workings of the pivot weir. Figure 5.4 plots all the calculated C_d for each inclination angle. The 90° weir behaves nearly identical to the previous study results, with a high C_d decreasing linearly until an almost constant value within the ideal-operating regime. The 72° weir has the lowest average C_d value and the value appears to increase as the angle decreases below 52°. At 47° and 27°, the C_d values are higher than that at 90° weir. The implications are further discussed in the following paragraphs.

Each angle of inclination also appears to have a region of *h/P* values where C_d is relatively constant. The constant region is likely indicative of an ideal-operating regime, as was found in the sharp-crested weir study. The findings further support the hypothesis that a single C_d value may be used with minimal error in the ideal-operating regime for a given gate angle under ideal conditions.

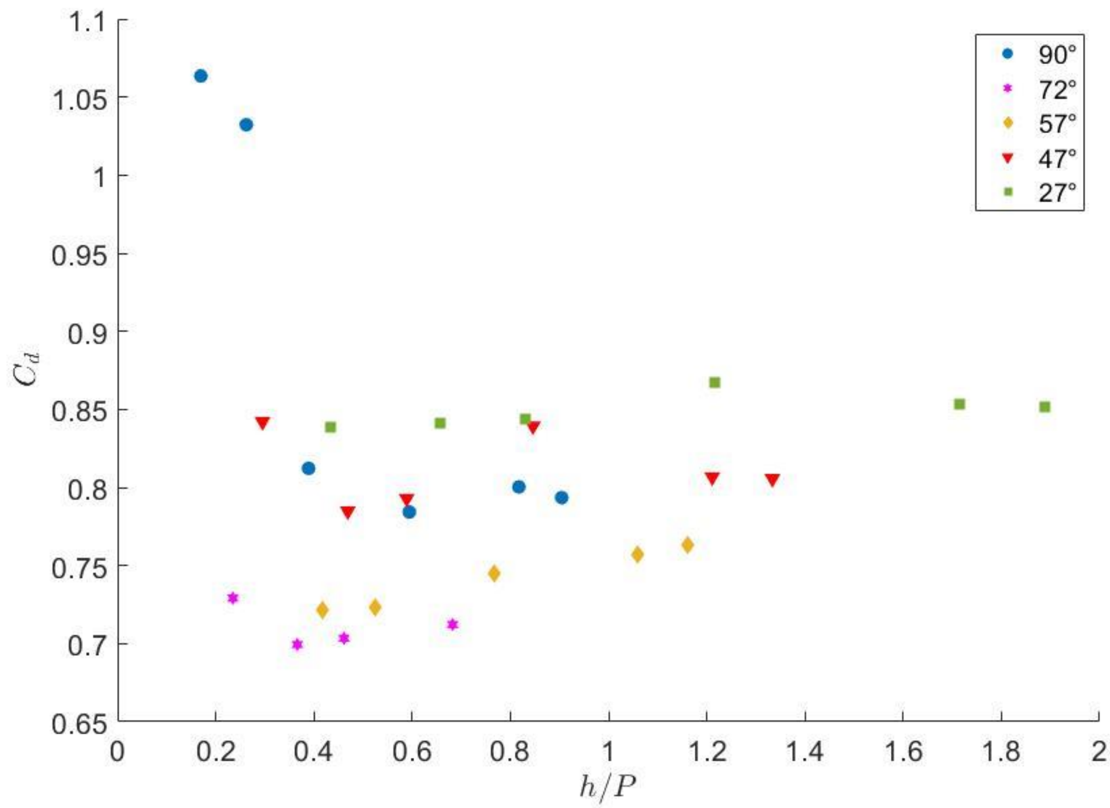

Figure 5.4 – C_d vs. *h/P* for each Pivot Weir Angle of Inclination.

A second analysis considered average C_d values for each gate angle to allow comparison to the sharp-crested weir study where it was proposed that a single C_d value could be used in the ideal-operating regime. Plotting the average C_d values together, Figure 5.5 provides a better visualization for how flow changes with a change in weir inclination angle. The highest average C_d value occurs at the lowest angle of inclination. Logically, the lower angles should be more efficient as the flow can more easily navigate over the weir without substantial alteration of the velocity vectors. However, for angles between 50° and 90°, the C_d value actually decreases. The decrease in C_d means flow over the weir crest is not acting as a jet flow or flow through a conduit, which is an inherent assumption in deriving the rating equation.

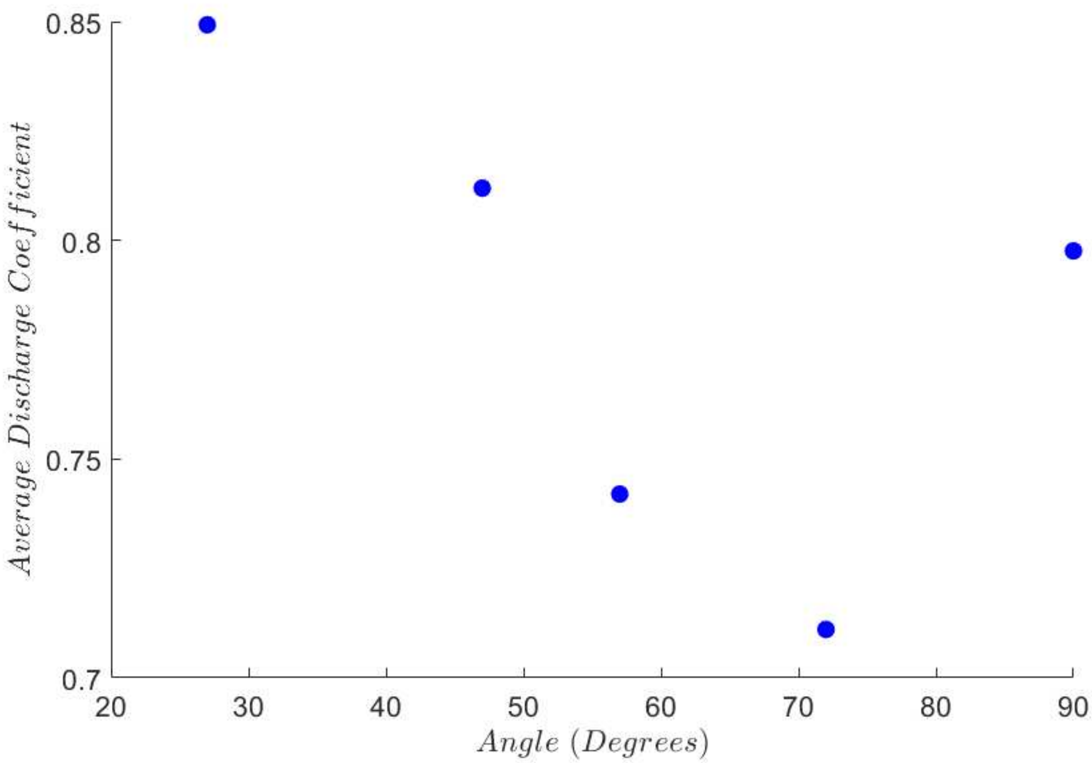

Figure 5.5 - Average C_d for Varying Pivot Weir Angles of Inclination.

Non-dimensional pressure and velocity profiles over the weir crest were plotted in Figure 5.6 for Q = 5.895 L/s for each weir inclination angle. The profiles were made non-dimensional in the same manner as the sharp-crested weir study. The linear line in the pressure plot represents a hydrostatic distribution. As the inclination angle decreases, the relative velocity over the crest increases which results in a corresponding decrease in relative pressure. This result is consistent with the earlier findings that the velocity head increases as inclination angle decreases. At the 47° angle, velocity accelerates over the weir crest, resulting in negative relative pressure. However, this result is not seen in the 27° inclination angle results. The lack of this expected trend is likely due to the resolution in the model. In the 27° inclination angle, larger changes in velocity and pressure occur over smaller distances. The current model mesh resolution is unable to capture these changes, making the results slightly skewed at the weir crest. A finer mesh resolution would likely reveal that the 27° weir would also have an acceleration zone and negative pressure region. The negative relative pressure region may also explain the collapsed nappe in the 47° and 27° inclination angle simulations. Fluid near the nappe is pulled down due to the negative pressure force which ultimately collapses the nappe.

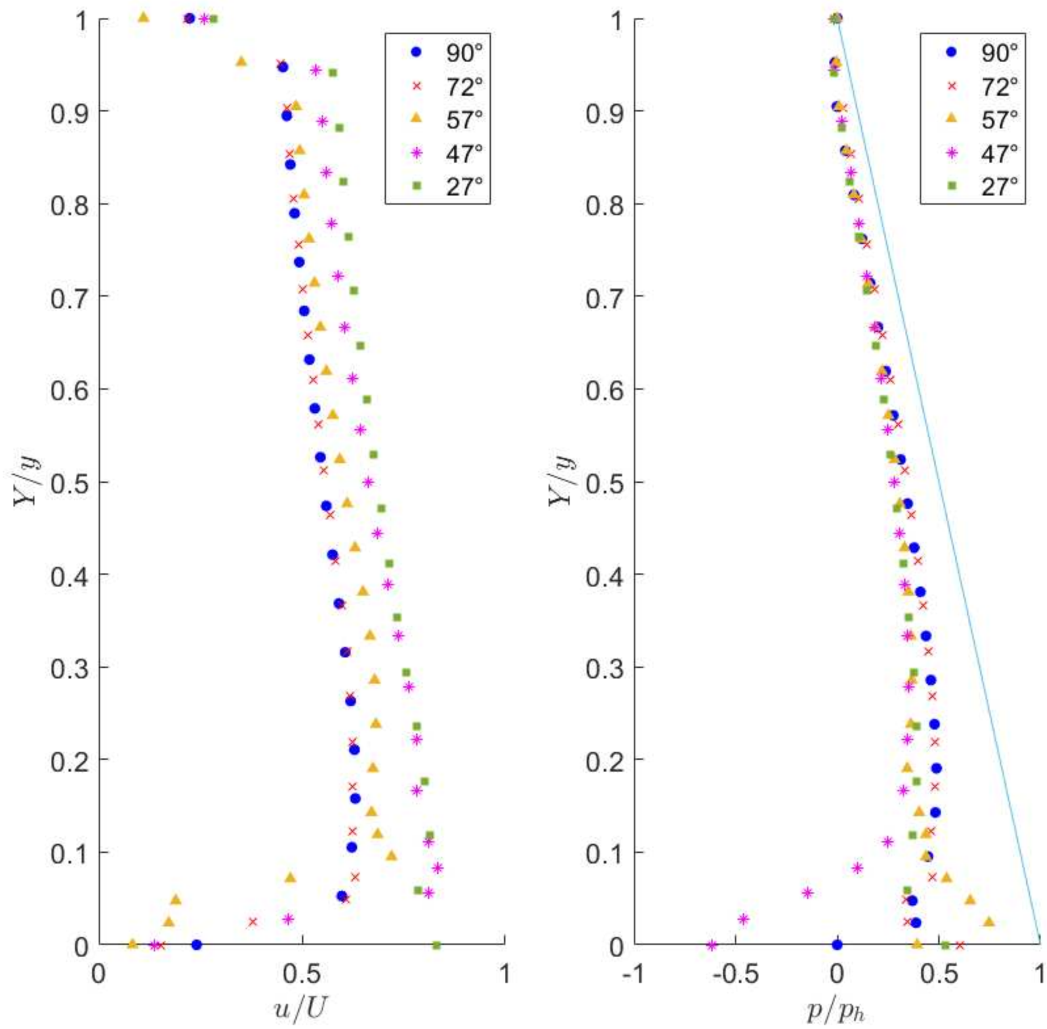

Figure 5.6 - Non-Dimensional Velocity and Pressure Profiles Over the Pivot Weir Crest for Q = 5.858 L/s.

Changes can also be seen in the velocity and pressure contours surrounding the weir. Figures 5.7 through 5.9 are series of such contour plots from each angle of inclination for Q = 5.895 L/s. The *x*- and *y*-velocity components (horizontal and vertical) are shown in Figures 5.7 and 5.8 respectively, as well as the pressure in Figure 5.9 as colored contours. The regions in warmer colors, such as red or yellow, indicate high *x*-velocities relative to that specific simulation. The dark blue is negative velocity in the vertical direction and yellow/green is zero vertical velocity.

Dark blues and cool colors are lower velocities. Similarly, high pressure is depicted with warm colors and low pressure with cool colors.

As the angle of inclination decreases, the *x*-velocity approaching the weir increases. For the 90° weir, the flow directly upstream of the weir must gain a vertical component in order to navigate over the weir. The vertical component of velocity is significant until the 47° weir, where the angle of inclination is low enough that the velocity does not need to change its vector significantly to flow over the weir. The turbulent recirculation zone near the weir can be seen moving from the upstream to the downstream side of the weir. In the 90° - 57° inclination angle, the recirculation zone appears upstream of the weir, while at an inclination angle < 57°, the region is only downstream of the weir. In the *y*-velocity contours, the vertical velocity is low surrounding the weir with the exception of the crest region. At the weir crest there is a significant vertical velocity component as the flow is propelled off the weir, sometimes resulting in the formation of a nappe at the high inclination angles. The pressure upstream of the base of the weir is hydrostatic, but the distribution changes as the inclination angle changes. As the weir inclination angle decreases, fluid must directly flow over the face of the weir. One additional note on the 47° inclination angle weir is the region of low pressure near the weir crest. A dark-blue region can be seen, indicative of the negative pressure section seen in the non-dimensional pressure profiles.

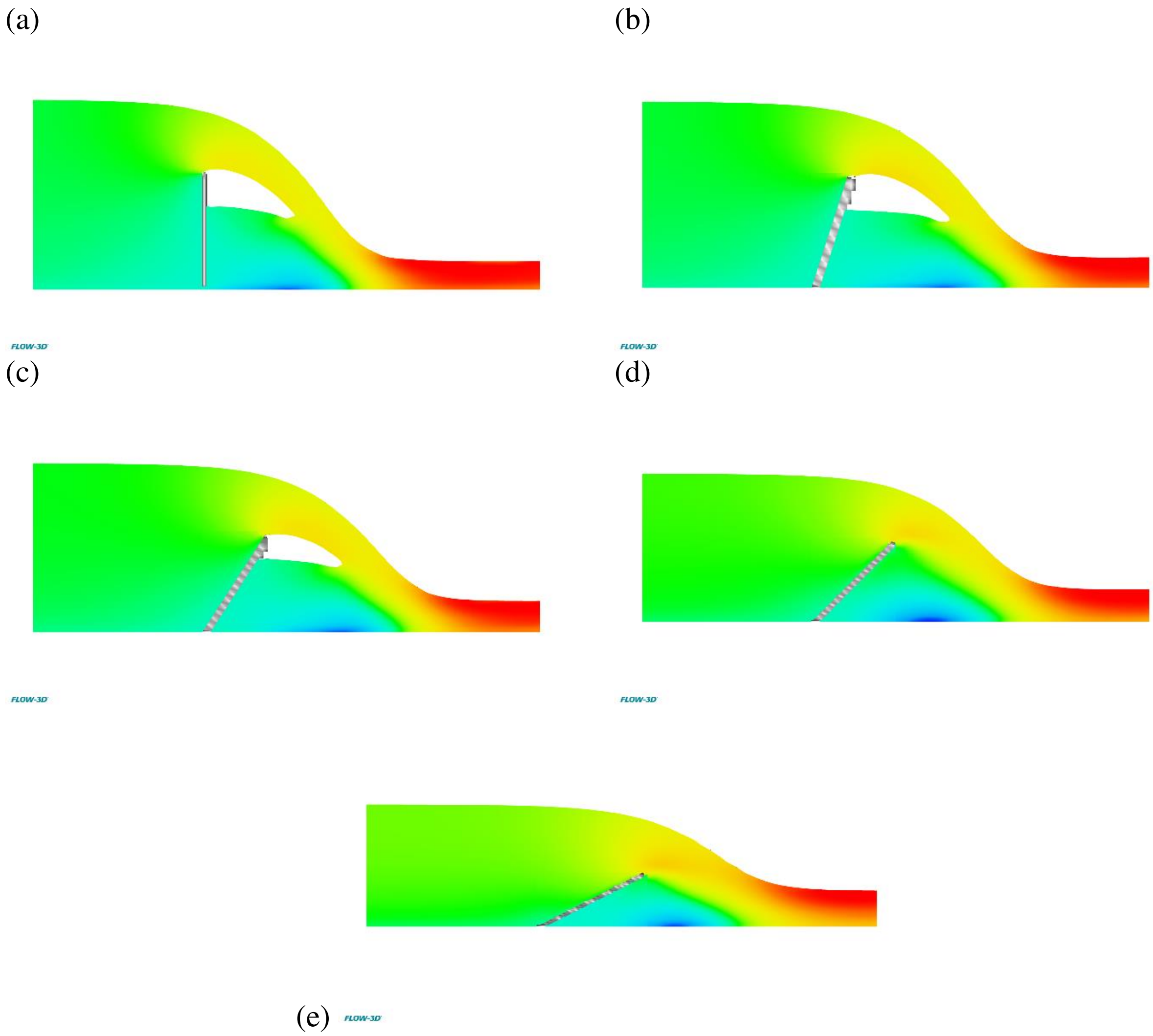

Figure 5.7 - x-Velocity Contours for Pivot Weir Study for Q = 5.895 L/s for (a) 90°, (b) 72°, (c) 57°, (d) 47°, and (e) 27°.

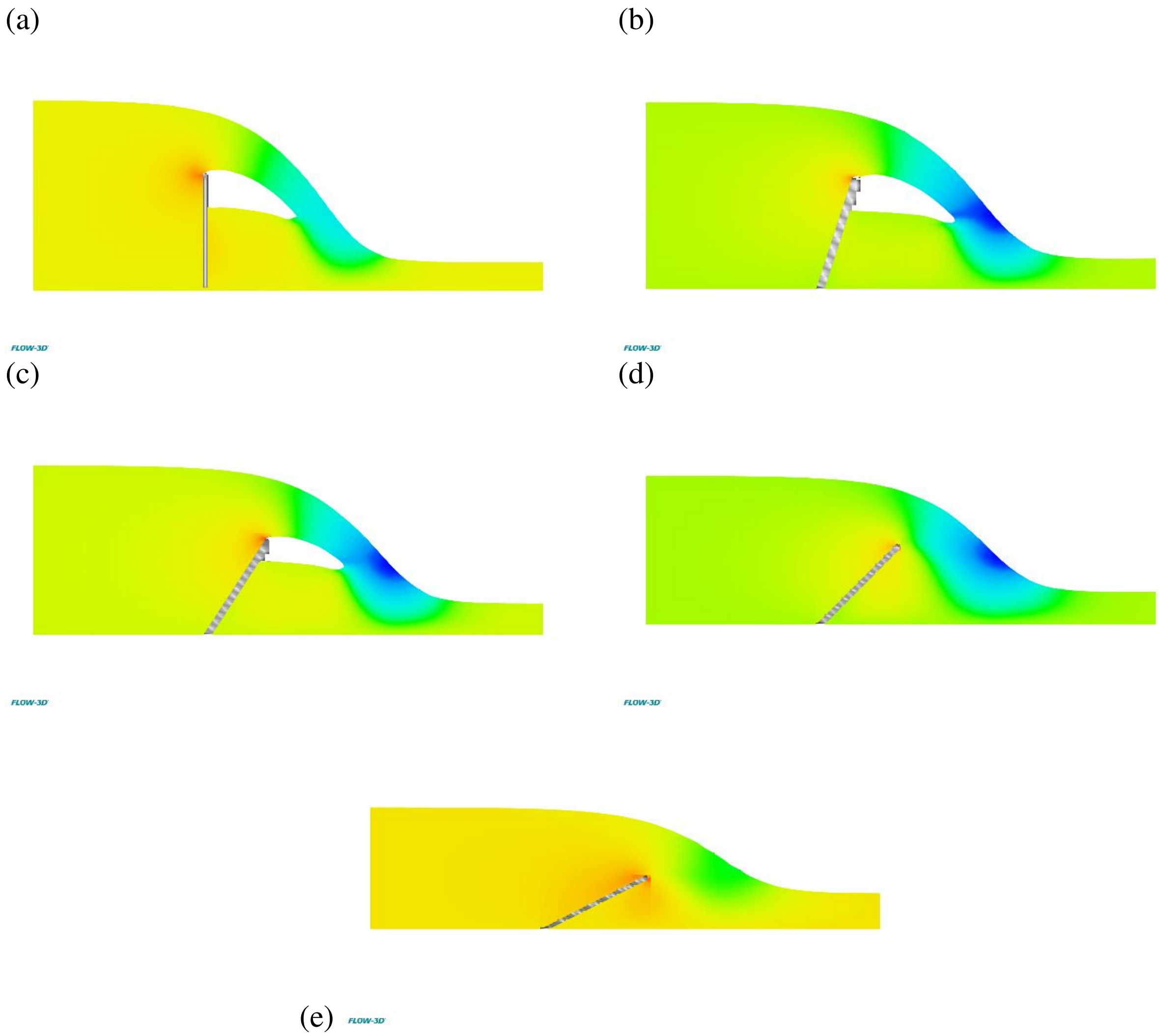

Figure 5.8 - *y*-Velocity Contours for Pivot Weir Study for Q = 5.895 L/s for (a) 90°, (b) 72°, (c) 57°, (d) 47°, and (e) 27°.

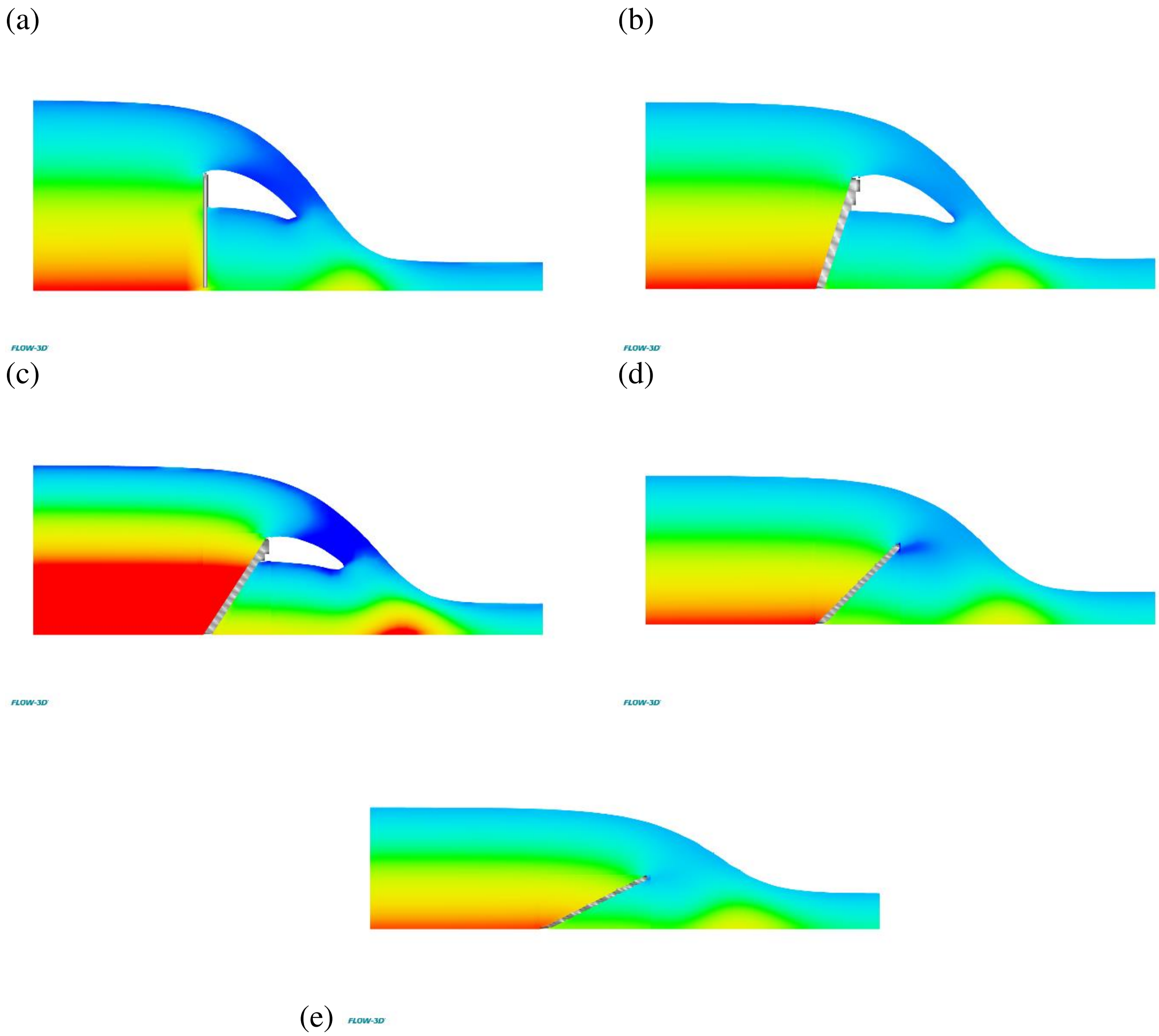

Figure 5.9 - Pressure Contours for Pivot Weir Study for Q = 5.895 L/s for (a) 90°, (b) 72°, (c) 57°, (d) 47°, and (e) 27°.

5.5 – Conclusion of the Pivot Weir Study

A parametric study using five different inclination angles and six flow rates was done using CFD to try to better understand how a pivot weir functions so that it might be used to its full potential. For a given flow rate, *h/P* increases as the angle decreases. The average percent of the upstream total mechanical energy head made up of the velocity head also increases with lower angles, meaning the *H/P* ratio will increase as well. The flow rates bounding the ideal-operating regime shift lower in magnitude as the inclination angle decreases. The value of the discharge coefficient remains relatively constant within the ideal-operating regime for each angle. Comparison of the average discharge coefficient for each angle reveals that at 57° and 72° the values are actually lower than at 90° coefficient. Studies are needed to examine this further. Velocity and pressure contours visually show how the flow surrounding the weir changes with change in inclination angle. As angle of inclination decreases, the *x*-velocity increases. The recirculation zone upstream of the weir disappears at 47°. Pressure upstream of the base of weir tends to be hydrostatic with low pressure regions in the nappe. Non-dimensional velocity and pressure profiles over the weir crest show that relative velocity increases as the angle of inclination decreases. The acceleration of velocity results in negative pressure for the 47° inclination angle simulation. The negative pressure may explain the disappearance of the nappe for this simulation. The linear pressure distribution continues over the weir face until close to the weir crest.

CHAPTER 6 – CONCLUSION, FUTURE WORK, AND CLOSING REMARKS

6.1 – Conclusion

The purpose of this study was to re-examine the sharp-crested weir and the pivot weir using CFD to better understand how they control and regulate flow in open channels. CFD was selected as the primary study tool because of its versatility and ability to simulate details of complex flow. Prior to studying either weir, several preliminary investigations were done to determine the best-practices for creating a model in the specific CFD code chosen, FLOW-3D. It was found that, due to the boundary condition specifications available in FLOW-3D, additional length upstream of the weir had to be provided to allow flow to fully-develop. Special care also had to be given to the height of the first computational cell adjacent to the bottom of the model domain to ensure accurate velocity profiles. The model length downstream of a freely flowing sharp-crested weir was varied to determine whether it had an impact on the upstream flow in the simulations. The downstream depth was found to have no effect so long as it did not intercept the nappe region.

A sharp-crested weir parametric study analyzed simulated velocity and pressure profiles over the weir crest, discharge coefficients, and turbulence structures upstream of the weir. Analysis of the profile and discharge coefficients revealed three distinct operating regimes dependent on h/P: the high-acceleration regime, ideal-operating regime, and the weir-inundated regime. In the high-acceleration regime, flow experiences acceleration in approaching the weir crest which results in low pressure. The ideal-operating regime is free from acceleration or inundation that violate the assumptions made in the derivation of the classical rating equation. In the weir-inundation regime, the weir begins to lose its influence as a control structure and is often submerged. The behavior of the discharge coefficients for the rating equation is also indicative of these regimes. In the ideal-operating regime, the discharge coefficient becomes relatively constant and it was concluded that a single value could be used for the flows in this regime with minimal error. Turbulence structures upstream of the weir showed a correlation to the upstream Reynolds number with a minimum eddy size occurring at about $Re = 70{,}000$.

The pivot weir study consisted of testing five different angles at six flow rates. It was found that the flow rates bounding the ideal operating regime decrease in magnitude with a decrease in inclination angle. For a given Q, the h/P value increases as the inclination angle decreases. Furthermore, the percent velocity head that comprises the upstream total mechanical energy head also increases as inclination angle decreases. Similar to the sharp-crested weir's ideal operating regime, the discharge coefficient for the pivot weirs were relatively constant in their own respective ideal-operating regimes. The averaged coefficients compared to one another indicated that the minimum discharge coefficient value was at 72° and the maximum value at 27°. However, further studies should be done to confirm and expand on this finding. Contours of velocity and pressure can indicate how the flow structure changes as the angle changes, with increases and decreases in different velocity components as well as the location of the turbulent recirculation region. Non-dimensional velocity and pressure profiles over the weir crest showed that relative velocity increases as the angle of inclination decreases. The increase in velocity due to an acceleration also causes a negative pressure region at the weir crest for the 47° inclination angle. The negative pressure may explain the collapsed nappe in the lower inclination angle simulations.

6.2 – Future Work

A number of topics that remain to be explored in the future. For both the sharp-crested and pivot weirs, 3D models could be applied to analyze how channel contractions or lateral flow might impact the results. It is expected that lateral flow should be negligible in a relatively straight channel, but otherwise may lead to more rich and developed turbulence patterns in the region surrounding the weir. A 2D model will not be able to develop the rich 3D structure of the recirculation eddy upstream of the weir, so eddy size results may be impacted by this. Also, in the field, weirs are typically placed immediately downstream of a channel contraction, in which case the geometry might have more distinct effects on flow over the weir. A 3D model would be able to better capture the effects of geometry on the flow as the contraction now introduces significant lateral flow.

Additional models should be built at scales representative of weirs in the field. The current CFD studies were run in conjunction with a laboratory study and field observations. The ultimate goal is a more coordinated linkage of the three approaches. Creating CFD models at the field scale inspired by real weirs used in irrigation canals would allow for further discoveries. Rough or irregular channel geometries as well as increased flow rates and more complex weir geometries can be created. Channel curves or contractions in the vicinity of the weir could also be modeled more easily at this scale and allowing for a validation of FLOW-3D for field scale conditions. Utilizing 3D models in field scale studied would also provide more accurate results as the amount of lateral flow increases with the complex geometry structures.

For the sharp-crested weir study, it would be advised to run higher *h/P* simulations in the A series of experiment setup to eliminate the possible impacts of a change in model geometry and resolution. The discharge coefficient values and profiles over the weir crest could be better analyzed and potentially provide more information. Further measurements of the eddy size could also be taken to identify how it continues to change as *h/P* increases.

For the pivot weir study, the scale of the models should be increased to dampen the potential influences of viscosity on the flow. Although the results did not appear to be influenced much by viscous forces, it would be best to diminish such effects as much as possible. Increasing the model scale would also allow the weir geometry to be more easily resolved without reducing the mesh to increasingly small scales. Furthermore, a validation between the pivot weir results and established laboratory experimental results should be done. A possible option for this is to validate the observed nappe structure reported in Wahlin and Replogle (1994).

Once a pivot weir geometry can be validated, a parametric study varying Q and analyzing similar results to the previous parametric study can be done. Simulating more flow rates will provide conclusive evidence to the hypothesis about the ideal-operating regime for varying angles of inclination. The discharge coefficient can be further analyzed and potentially broken into two components: a coefficient dependent on the derivation assumptions for the rating equation and a coefficient dependent on the effects of the inclination angle. The geometry of the pivot weir can then be changed to match that of an Obermeyer weir to study the effects of a curved weir leaf on flow over the weir.

6.3 – Closing Remarks

The sharp-crested weir and pivot weir are useful hydraulic structures whose versatility and reliability have made them popular around the world. Despite the body of work previously conducted on the sharp-crested weir, there are still aspects yet to be explored. The pivot weir remains a relatively new subject of research that would benefit from future studies. Understanding how these structures work to control and measure open-channel flow and how they can be better implemented will improve water management and help reduce the water crisis. Expanding these types of CFD studies to even more hydraulic structures, such as sluice gates, flumes, or drops, will push water engineering knowledge further forward. All of this together can help make the world's water supply less restrictive and hopefully improve conditions in regions where water is scarce. Enhancing understanding of fluid mechanics and hydraulics will remain a vital component to making the world a better place.

REFERENCES

"Pneumatically Actuated Gates." (n.d.). *Pneumatically Actuated Gates | Obermeyer Hydro, Inc.*, <http://www.obermeyerhydro.com/SpillwayGates> (May 4, 2021).

"weir." (n.d.). *Wiktionary*, <https://en.wiktionary.org/wiki/weir> (Jun. 24, 2021).

Bates, P. D., Lane, S. N., and Ferguson, R. I. (2005). "Computational Fluid Dynamics Modelling for Environmental Hydraulics." *Computational Fluid Dynamics*, 1–15.

Bayon, A., Valero, D., García-Bartual, R., Vallés-Morán, F. J., and López-Jiménez, P. A. (2016). "Performance assessment of OpenFOAM and FLOW-3D in the numerical modeling of a low Reynolds number hydraulic jump." *Environmental Modelling & Software*, 80, 322–335.

Bijankhan, M., and Ferro, V. (2018). "Experimental Study and Numerical Simulation of Inclined Rectangular Weirs." *Journal of Irrigation and Drainage Engineering*, 144(7), 04018012.

Bijankhan, M., and Ferro, V. (2020). "Experimental Modeling of Submerged Pivot Weir." *Journal of Irrigation and Drainage Engineering*, 146(3), 04020001.

Bos, M. (1976). *Discharge Measurement Structures*. Wageningen: ILRI.

Ferrari, A. (2010). "SPH simulation of free surface flow over a sharp-crested weir." *Advances in Water Resources*, 33(3), 270–276.

Flow Science (2021). *FLOW-3D User Manual*, Release 12, Flow Science Inc., Santa Fe, NM.

Henderson, F. M. (1964). *Open channel flow*. Prentice Hall, Upper Saddle River, NJ.

Hirt, C. W. (1993). “Volume-fraction techniques: power tool for wind engineering.” J. Wind Engng. Ind. Aerodyn., 46-47, 327-338.

Hirt, C. W., and Nichols, B. D. (1981). “Volume of fluid (VOF) method for the dynamics of free boundaries.” J. Comput. Phys., 39, 201-225.

Horton, R. (1907). “Weir experiments, coefficients, and formulas (revision of Water-Supply Paper 150).” *Water-Supply and Irrigation*, M, (200).

Johnson, M. C. (2000). “Discharge coefficient analysis for flat-topped and sharp-crested weirs.” *Irrigation Science*, 19(3), 133–137.

Kindsvater, C. E., & Carter, R. W. (1959). Discharge characteristics of rectangular thin-plate weirs. *Transactions of the American Society of Civil Engineers*, 124(1), 772-801.

M.S. Prakash, M. Ananthayya, G.M. Kovoor (2011) “Inclined rectangular weir-flow modeling.” J. Earth Sci. India, 4(2), 57-67

Mahdavi, A., and Shahkarami, N. (2020). “SPH Analysis of Free Surface Flow over Pivot Weirs.” *KSCE Journal of Civil Engineering*, 24(4), 1183–1194.

N. Rajaratnam & D. Muralidhar (1971) Pressure And Velocity Distribution For Sharp-Crested Weirs, *Journal of Hydraulic Research*, 9:2, 241-248, DOI: 10.1080/00221687109500348

Pope, S. B. (2000). *Turbulent flows*. Cambridge University Press, Cambridge.

Qu, J., Ramamurthy, A. S., Tadayon, R., and Chen, Z. (2009). “Numerical simulation of sharp-crested weir flows.” *Canadian Journal of Civil Engineering*, 36(9), 1530–1534.

Ramamurthy, A. S., Tim, U. S., and Rao, M. V. (1987). “Flow Over Sharp-Crested Plate Weirs.” *Journal of Irrigation and Drainage Engineering*, 113(2), 163–172.

Rehbock, T. (1929). “Discussion of Precise Measurements". *Trans. of ASCE*, 93, 1143-1162

Sotiropoulos, F. (2005). “Introduction to Statistical Turbulence Modelling for Hydraulic Engineering Flows.” *Computational Fluid Dynamics*, 91–120.

Swamee, P. K. (1988). “Generalized Rectangular Weir Equations.” *Journal of Hydraulic Engineering*, 114(8), 945–949.

Takouleu, J. M. (2020). “EGYPT: Lining irrigation canals to save 5 billion m^3 of water.” *Afrik 21*, <https://www.afrik21.africa/en/egypt-lining-irrigation-canals-to-save-5-billion m%C2%B3-of-water/> (Jun. 23, 2021).

Tracy, H. J. (1957). Discharge characteristics of broad-crested weirs (Vol. 397). *US Department of the Interior*, Geological Survey.

Versteeg, H. K., and Malalasekera, W. (2011). *An introduction to computational fluid dynamics: the finite volume method*. Pearson Education, Harlow.

Wahlin,B. T., & Replogle, J. A. (1994). Flow measurement using an overshot gate. Phoenix, AZ: UMA Engineering.